

1 **Controls over particle motion and resting times of coarse bed load transport in a**
2 **glacier-fed mountain stream**

3
4 Luca Mao^{1,2}, Matteo Toro³, Ricardo Carrillo⁴, Francesco Brardinoni⁵, Luigi
5 Fraccarollo³
6

7 ¹ School of Geography, University of Lincoln, Brayford Pool, LN6 7TS, Lincoln, UK.

8 ² Institute of Geography, Pontificia Universidad Católica de Chile, O'Higgins 340,
9 Santiago, Chile.

10 ³ Department of Civil, Environmental and Mechanical Engineering, University of
11 Trento, Via Mesiano 77, 38123, Trento, Italy.

12 ⁴ Department of Ecosystems and Environments, Pontificia Universidad Católica de
13 Chile, O'Higgins 340, Santiago, Chile.

14 ⁵ Department of Biological, Geological and Environmental Sciences, University of
15 Bologna, Via Zamboni 67, 40126, Bologna, Italy.

16
17 Corresponding author: Luca Mao, lumao@lincoln.ac.uk
18

19 **Abstract**

20 Coarse bed load transport is a crucial process in river morphodynamics but is difficult to
21 monitor in mountain streams. Here we present a new sediment transport dataset obtained
22 from two years of field-based monitoring (2014-2015) at the Estero Morales, a high-
23 gradient stream in the central Chilean Andes. This stream features step-pool bed geometry and
24 a glacier-fed hydrologic regime characterized by abrupt daily fluctuations in discharge. Bed
25 load was monitored directly using Bunte samplers and by surveying the mobility of PIT
26 (passive integrated transponder) tags. We used the competence method to quantify the effective
27 slope, which is the fraction of the topographical slope responsible for bed load transport. This
28 accounts for only 10% of the topographical slope, confirming that most of the energy is
29 dissipated on macroroughness elements. We used the displacement lengths of PIT tags to
30 analyze displacement lengths and virtual velocity of a wide range of tracer sizes (38-415 mm).
31 Bed load transport in the Estero Morales show to be size-selective and the distance between

32 steps influences the displacement lengths of PIT tags. Displacement lengths were also used to
33 derive the statistics of flight distances and resting times. Our results show that the average
34 length of flight scales inversely to grain size. This contradicts Einstein's conjecture about the
35 linear relationship between grain size and intervals between resting periods in a steep step-pool
36 stream in ordinary flood conditions.

37

38 **1. Introduction**

39 Sediment transport, flow resistance, morphological structure and bed texture in rivers
40 are interrelated in complex ways (Church, 2006). Coarse bed load transport in
41 mountain streams is important for civil engineers, geomorphologists, river ecologists
42 and managers, as it determines channel morphology and dynamics, while representing
43 a significant component of flood-related costs (e.g. Badoux et al., 2014). However,
44 monitoring bed load in the field can be logistically onerous, costly, and affected by a
45 number of uncertainties (Dell'Agnese et al., 2014; Schneider et al., 2016; Vericat et
46 al., 2006; Magirl et al., 2015).

47 Predicting bed load is a difficult task, especially in steep mountain streams, where
48 channel beds are often organized in boulder-cascade and step-pool morphologies
49 (Brardinoni & Hassan, 2007; Buffington & Montgomery, 1997; Comiti & Mao, 2012).
50 Modelling the flow over such bed structures is still very challenging (Saletti et al.,
51 2016; Escauriaza et al., 2017), especially when levels of submergence are low (Comiti
52 et al., 2009; Wilcox et al., 2011). Modeling flow and bedload transport in mountain
53 stream is complex because patches of mobile sediments coexist with immobile
54 structures such as steps or isolated boulders (Laronne et al., 2001; Green et al., 2015;
55 Yager et al., 2012). Furthermore, critical dimensionless shear stress in mountain
56 streams (i.e. Shields stress) is very difficult to model, due to its high variability in time
57 (Masteller et al., 2019) and space (Monsalve et al., 2016), modulated by changes in
58 local channel slope (Lamb et al., 2008) and relative submergence of sediments (Lenzi
59 et al., 2006).

60 Only part of the flow power in mountain streams is available to entrain and transport
61 sediments (Rickenmann & Recking, 2011; Hohermuth & Weitbrecht, 2018), as some
62 energy is dissipated in various ways, including local hydraulic plunging and jumps

63 over steps (Comiti et al., 2009; Green et al., 2013; Monsalve et al., 2017). In such
64 complex hydraulic conditions, well known and established flow resistance approaches
65 and empirical bed load formulas are unlikely to be reliable (e.g. Yager et al., 2018).
66 Considering that mountain streams are typically supply limited (Lenzi et al., 2004;
67 Turowski et al., 2009), bed load formulas fail to predict actual transport rates by orders
68 of magnitude in step-pool streams (Nitsche et al., 2011), since not all the energy
69 available is effective in transporting sediments. Because macroroughness can represent
70 up to 90 % of the total flow resistance in step-pool streams (Church & Zimmermann,
71 2007), accounting for the portion of energy slope or flow resistance associated with
72 macroroughness can substantially increase the predictive power of empirical bed load
73 formulas (Chiari & Rickenmann, 2011). Using a large empirical database,
74 Rickenmann & Recking (2011) adopted Ferguson's approach (2007) for partitioning
75 flow resistance and splitting the friction factor into a base level value associated with
76 small-scale grain size roughness, and total value, which includes macroroughness,
77 such as step-pools. A similar breakdown can be applied to the topographical bed slope
78 (i_b), from which an effective slope value (i_e) representing that part of the slope that
79 plays a role in coarse grain entrainment and movement can be extracted from the
80 remaining part of the slope ($i_b - i_e$) associated with the mechanical power dissipated by
81 flow over immobile bed forms (Nitsche et al., 2011).

82 Controls on sediment transport processes and dynamics in mountain streams can be
83 explored using tracers. Displacement lengths of tracers depend on particle size and
84 shear stress acting on them (e.g. Church & Hassan, 1992), but also on dimensionless
85 impulse (e.g. Phillips et al., 2013) and antecedent flow conditions (e.g. Mao et al.,
86 2017). Displacement length depends also on channel morphology and especially on
87 the spacing between bedforms (Vázquez-Tarrío et al., 2019). Displacement length is
88 needed to calculate the virtual velocity of sediment, that can be used to assess coarse
89 bed material transport (e.g. Brenna et al., 2019). Velocity is called virtual because it is
90 usually calculated considering the interval between two consecutive surveys of tracers.
91 However, tracers would naturally move through sequences of jumps and rest periods
92 (Einstein, 1950) that are observable in laboratory experiments (e.g. Fraccarollo &
93 Hassan, 2019) but difficult to monitor in the field, with only a few exceptions (e.g.

94 Habersack, 2001; Maniatis et al., 2017).

95 In this paper, we use a new dataset of direct bed load surveys in a step-pool stream to
96 calculate the portion of slope effective in transporting sediments. We then use this
97 slope value to analyze sediment transport dynamics, and apply the Einstein (1950)
98 and virtual velocity (Haschenburger & Church, 1998) approaches to characterize bed
99 load mobility. Both approaches are based on a Lagrangian perspective of sediment
100 transport which considers the motion of individual particles, and views moving grains as
101 being almost independent of each other. While sliding, rolling and saltating over the
102 bed, sediments may also experience long resting periods on the surface, or may be
103 temporarily buried as a result of temporal and spatial changes in the bed surface
104 profile (Singh et al., 2009; Wong et al., 2007). Both the Einstein and the virtual
105 velocity formulations allow for predicting bed load transport rates and can be expressed
106 as a function of Shields stress, such as the MPM empirical bed load formula (Meyer-
107 Peter & Muller, 1948; Wong & Parker, 2006). Here we will use field data to infer the
108 predictors of Einstein's statistical approach. The study was conducted at the Estero
109 Morales, a small glacier-fed Andean step-pool stream in central Chile. Coarse
110 sediment mobility and transport rates were monitored in 2014-2015 using Bunte traps
111 and Passive Integrated Transponders (PIT) tagged clasts. The specific aims of the
112 paper are to i) use the competence approach to assess energy dissipation in step-pool
113 morphology by calculating the effective slope of the stream; ii) use the effective slope
114 to assess the increase in the predictive power of a widely applied formula in a system
115 with nearly unlimited sediment supply; iii) use the virtual velocity of PIT tracers to
116 assess sediment mobility; and iv) assess the resting times of PIT tags using both
117 particles that moved during the survey period and those that did not.

118

119 **2. Study site and monitoring methods**

120 *2.1. Study site*

121 The study was conducted in a reach of the Estero Morales, a high-gradient stream in
122 the central Chilean Andes (Figure 1). The basin extends for 27 km², with an
123 elevation between 1780 and 4497 m.a.s.l. There are several relatively small glaciers
124 above 2700 m.a.s.l. (Mao & Carrillo, 2017). Mean annual rainfall, as measured in the

125 lower part of the basin, is around 550 mm. The climate is Mediterranean, with
126 precipitation occurring mainly as snowfall from April to September, with occasional
127 convective summer storms and late summer rain-on-snow events. The catchment is
128 covered by snow for approximately 5 months a year, so discharge mainly results from
129 snowmelt in late spring (from late September to November) and glacier melt from
130 December to March. Bedrock geology of the catchment consists of volcanic
131 metamorphic rock and conglomerate-sand deposits. The stream in the study reach is
132 steep (0.14 m/m) and the channel width is approximately 7 m. The study reach is
133 760 m long and is located just upstream from the confluence with the El Volcan
134 River (Figure 1). The stream flows through coarse lag deposits and features typical
135 of step-pool sequences (Figure 2). In 2015, we counted 72 step-pool units over the
136 760 m-long reach, with an average spacing of approximately 10.5 m. The step-pool
137 sequences are stable during ordinary glacial melting floods and are only prone to
138 dislodgement and rearrangement during extreme late summer events. The site was
139 monitored continuously from July 2013 until April 2016, when a high-magnitude
140 event caused considerable channel changes and destroyed the monitoring devices.
141

142 *2.2. Bed load monitoring and sampling using Bunte traps*

143 The study reach was equipped with a pressure transducer and a multiparameter water
144 quality probe (OTT Hydrolab MS5) to monitor water temperature, electrical
145 conductivity, and turbidity with a 10-min time resolution (see Mao & Carrillo, 2017).
146 A 0.5-m-long acoustic pipe sensor was also installed (Mao et al., 2016). A series of
147 direct bed load samples were collected near the monitoring cross-section using 0.3 m-
148 wide, 0.25 m-high Bunte-type traps (Bunte et al., 2004). Two traps were located at
149 points near the bed load acoustic pipe sensor (Figure 2), located on the sampling site
150 (Figure 1). Samples were collected during the glacier melting season (January to
151 March) in 2014 and 2015 at discharges ranging from 1 to 3 m³ s⁻¹. The highest
152 discharge monitored was roughly the bankfull discharge. The highest discharge in the
153 Estero Morales (approx. 7 m³ s⁻¹) was recorded in April 2016 and was able to destroy
154 and recreate step-pools (Mao & Carrillo, 2017). Samplings was concentrated in a few
155 days to monitor bed load at a wide range of transport rates. Multiple samples were

156 taken, especially during the rising limb of hydrographs. The duration of bed load
157 sampling ranged from 1 to 120 minutes depending on the discharge. The amount of
158 trapped sediment ranged from 0.1 to 49.7 kg. The sediment collected in the traps was
159 dried, weighed and later sieved in the laboratory.

160

161 *2.3. Bed load monitoring using tracers*

162 Coarse sediment mobility in Estero Morales was also investigated using natural clasts
163 equipped with 23-mm-long radio frequency identification (RFID) passive integrated
164 transponder tags (Hassan et al., 2013; Liebault et al., 2012). PIT tags are transmitters
165 without batteries that emit an identification codes by radio frequencies, which are
166 detected and recorded. The RFID PIT system uses electromagnetic fields to
167 automatically identify tags. A commercially available mobile RFID system
168 consisting of a reader unit, a battery supplying the system, a screen, and a short-range
169 antenna (0.5 m in diameter), was used to determine the position of PIT tags (Figure
170 2). The antenna can generally recognize tracers in a range of 0.3 m, although this
171 varies depending on the position of the clast relative to the antenna, the battery charge,
172 and interference among PIT tags (see Chapuis et al., 2014).

173 PIT tags were inserted in holes drilled in the clasts and closed using epoxy glue. The
174 three main dimensions of the clasts (a – long, b – medium, c – short) were measured
175 with a caliper and the clasts were weighed to determine the relationship between b-
176 axis diameter and weight. Only sediments collected in the Estero Morales were used
177 to produce PIT tracers for this study. The tracers were also spray-painted to enhance
178 their visibility in the channel bed. The PIT tags were placed in the upstream end of
179 the study reach and ended up at the confluence with the El Volcan River. As in other
180 studies (e.g. Dell’Agnese et al., 2015), the PIT tags were laid in the channel bed and
181 gently pushed by foot into the surface sediment material to prevent them from
182 protruding abnormally from the bed. PIT tags were always inserted at three transects
183 (spaced 0.5 m apart) at the upstream end of the reach. The operator equipped with
184 the mobile antenna scanned the channel bed surface for tags. When a tag was
185 detected, vertical and horizontal distance were measured from wooden stakes with a
186 laser rangefinder. Overall, 32 wooden stakes were located along the study site, and

187 all were georeferenced using DGPS. At the beginning of the measuring periods in
188 January 2014 and January 2015, 461 and 395 PITs respectively were placed in the
189 study reach during low-flow conditions. PIT positions were surveyed 20 times in 2014
190 and 13 times in 2015. Each survey took one to two days, and required intense in-
191 channel surveys, carried out by two operators, who worked until 2 PM, after which
192 increased discharge made the search for PITs unsafe. The flow regime during the
193 monitoring search for PITs was always characterized by daily fluctuations in
194 discharge. The surveys always started from the upstream end of the monitored reach.
195 Due to the rapid increase in water discharge in the early afternoon, it was generally
196 possible to survey only the upper half of the reach. On one occasion, it was possible to
197 survey the entire reach. Figure 3 shows the size distribution of the tracers, and the bed
198 surface and subsurface sediments. A surface grid-by-number sampling revealed that
199 the sediments are coarse and poorly sorted ($D_{16} = 20$ mm; $D_{50} = 59$ mm; $D_{84} = 318$
200 mm; $D_{90} = 448$ mm; Figure 3). A volume-by-weight subsurface sampling showed that
201 bed material grain size distribution is finer than that of the surface, demonstrating a
202 certain rate of surface armoring ($D_{50-sub} = 25$ mm; Figure 3). The b-axes of tracers
203 range from 27 to 420 mm. The lower value of this range was determined by the length
204 of the PIT tags inserted in the clasts (23 mm), and the upper value by the size of
205 pebbles in which PITs could be inserted and then transported in the study site.

206

207 **3. Conceptual and theoretical framework: unifying the statistical motion and** 208 **virtual velocity approaches**

209 In this section, we introduce Einstein's (1950) bed load formula, and present the way
210 field data collected with the PIT tracers was used to back-calculate the predictors that
211 appear in the formula. Einstein's pioneering approach describes the bed load transport
212 rate as a function of two predictors that consider the probabilistic distribution of mean
213 particle displacements \bar{L} and $\overline{T^{-1}}$, being T the resting time. L represents the distance
214 that a particle runs without pausing during its movement from an entrainment to the
215 subsequent deposition. We refer to this as flight distance, whereas in other studies (e.g.
216 Bradley et al., 2010; Habersack, 2001; Nikora et al., 2002) it is termed step or travel
217 distance, quick length step, intermediate trajectories, and travel distance. T is the

218 resting time, i.e. the time interval from a first deposition to the next entrainment,
 219 whereas T^l represents the probability for a single grain at rest to be entrained in a unit
 220 of time. The Einstein expression has two further factors, which are constant for a given
 221 bed, i.e. the number N of grains paving a unit area and the reference volume V of a
 222 single particle. N can be evaluated as the ratio between bed particle concentration c_b
 223 (volumetric percentage of solid volumes) and the particle reference cross section A .
 224 Following the above notations, the Einstein (1950) formulation for the unit volumetric
 225 transport rate q_s (in m^2/s) is expressed as:

$$226 \quad q_s = \overline{T^{-1}} \forall \frac{c_b}{A} \overline{L} \quad (1)$$

227 In order to make Eq. 1 applicable to all i^{th} grain size classes of a poorly sorted mixture,
 228 we add a factor f_i , which indicates the volumetric frequency of the class size D_i ,
 229 resulting in:

$$230 \quad q_{si} = \overline{T_i^{-1}} \forall_i \frac{c_b}{A_i} \overline{L}_i f_i \quad (2)$$

231 where V_i is the reference volume of a single particle in the i^{th} grain size class. The term
 232 $\overline{T_i^{-1}} \frac{c_b}{A_i}$ can be termed E_i , which represents the number of particles entrained per unit of
 233 time and unit of bed-surface area. Unless the probability distribution of the resting
 234 times is uniform, it holds that:

$$235 \quad \overline{T_i^{-1}} \neq \frac{1}{T_i} \quad (3)$$

236 The ratio \forall_i/A_i is equal to αD_i , α being a constant. Indeed, for nearly spherical-shaped
 237 grains it holds that $\forall_i/A_i = \frac{4}{3} \pi \frac{D_i^3}{8} / \pi \frac{D_i^2}{4} = \frac{2D_i}{3}$. Thus, it is generally true that α is close
 238 to unity and depends on the shape of the particle. Eventually, Eq. 2 becomes:

$$239 \quad q_{si} = \alpha D_i c_b \overline{T_i^{-1}} f_i \overline{L}_i \quad (4)$$

240 The distribution of T_i can be obtained from the dataset collected in the field using the
 241 tracers (see Section 6).

242 The unit volumetric transport rate q_s (per unit of width of the active channel) in the
 243 virtual velocity approach can be calculated for well sorted sediments as follows
 244 (Haschenburger & Church, 1998; Liebault & Laronne, 2008; Hassan & Bradley,
 245 2017):

$$246 \quad q_s = V_v \delta c_b \quad (5)$$

247 where c_b is the volumetric concentration of the sediments in the bed and δ is the
 248 thickness of the active layer of sediments. The virtual velocity of bed load V_v is
 249 calculated as the ratio between the total displacement ℓ travelled by a particle in a
 250 certain time interval t , and t itself. Because particles are entrained, move and rest
 251 several times during a transport event, it holds that t is much longer than the above
 252 defined T and that the total displacement ℓ is much longer than the previously
 253 defined \bar{L} . Virtual velocity V_v is thus the averaged velocity, over both motion and
 254 resting periods, of a large ensemble of grains running their trajectory. The transport
 255 of each i^{th} grain size fraction of a poorly sorted bed mixture, given its volumetric
 256 fraction f_i in the bed mixture, and its representative grain size D_i , is given by:

$$257 \quad q_{si} = V_{vi} \delta c_b f_i \quad (6)$$

258 In this paper, we use the data collected with PIT tracers in sequential surveys to
 259 calculate the virtual sediment velocity V_v , calculating T_T as the time elapsed from
 260 when a trace was inserted in the bed (or the previous survey) until the last time it was
 261 detected, and l_T as the distance traveled from the release (or the previous survey) to
 262 the position at which it was last recovered (as is usually done in literature, see
 263 Vasquez-Tarrio et al., 2019). From Eq. (6) it can be drawn that:

$$264 \quad V_{vi} = q_{si} / c_b \delta f_i \quad (7)$$

265 With the aim of establishing a relation between the two approaches, Eqs. 2 and 7 can
 266 be combined as:

$$267 \quad q_{si} = \alpha D_i c_b \overline{T_i^{-1}} f_i \bar{L}_i = V_{vi} \delta c_b f_i \quad (8)$$

268 Eq. 8 yields:

$$269 \quad V_{vi} \approx \overline{T_i^{-1}} \bar{L}_i \frac{\alpha D_i}{\delta} \quad (9)$$

270 which displays a straightforward interpretation of virtual velocity in terms of
 271 predictors in Einstein's approach. Interestingly, Eq. 9 applies to both well and poorly
 272 sorted bed mixtures.

273

274 **4. Effective slope and predictive power of empirical bed load formulas**

275 Around two thirds of the total energy in steep streams can be dissipated in the
 276 hydraulics generated by step-pool sequences (e.g. Wilcox et al., 2011), and this
 277 dissipated energy does not contribute to generating bed load transport. Here we apply

278 a slope decomposition approach (as in Nitsche et al., 2011), in which the mean
 279 topographic longitudinal slope i_b is split into the effective slope involved in sediment
 280 transport (i_e) and the component of slope that is absorbed in form and spill drags (i_f):

$$281 \quad i_b = i_e + i_f \quad (10)$$

282 To calculate the effective slope i_e , we used the competence approach for incipient
 283 sediment motion, which considers the largest particle transported and collected during
 284 bed load samplings conducted under different hydrometric conditions (Andrews, 1983;
 285 Batalla & Martin-Vide, 2001; Mao et al., 2008). In the case of the Estero Morales, we
 286 used the size of the coarsest grain captured with the Bunte traps (D_{100}) and the shear
 287 stress acting on the bed calculated using the depth-slope approach (Wilcock, 1993),
 288 which involves the use of the water depth at the time of sampling (h), topographical
 289 slope (i_b), the acceleration constant due to gravity (g) and water density (ρ). The shear
 290 stress associated with sediment transport is calculated as:

$$291 \quad \tau = h i_b g \rho \quad (11)$$

292 Here we adopted the flow competence method, which assumes that the local flow
 293 conditions at the moment of bedload sampling can be considered critical for the
 294 entrainment and transport of the coarsest sediment trapped in the sampler (Andrews,
 295 1983; Lenzi et al., 2006). In other words, the shear stress during a bedload sampling is
 296 critical for the coarsest particles found in the Bunte trap (D_{100}), and thus the critical
 297 Shields stress (θ_{cr}) can be calculated as:

$$298 \quad \theta_{cr} = \frac{h \cdot i_b}{\Delta \cdot D_{100}} \quad (12)$$

299 where $\Delta = \rho_s / \rho - 1$ and ρ_s is the density of sediments. If i_e , rather than i_b , is
 300 considered in Eq. 12, the effective slope can be calculated as:

$$301 \quad i_e = \frac{\theta_{cr} \cdot \Delta \cdot D_{100}}{h} \quad (13)$$

302 which shows that the ratio D_{100}/h is proportional to i_e , provided that θ_{cr} is assumed to
 303 be constant. Figure 4 shows the relationship between transported D_{100} and the water
 304 depth at the time of direct bed load sampling conducted in 2014 and 2015. The size of
 305 the coarsest transported sediments increases with the flow depth, although the
 306 predictive power of a linear regression is very weak ($R^2 = 0.29$). The considerable
 307 scatter of data is consistent with previous observations (e.g., Mao et al., 2008). On the
 308 one hand, this could be attributed to the reduced trapping efficiency of Bunte

309 samplers, especially at higher bed load transport rates due to shorter sampling times
310 and the fact that D_{100} approaches the size of the sampler intake. On the other hand, the
311 scatter observable in Figure 4 is also due to the natural grain size variability of
312 upstream sediment delivery sources, dynamics of destruction of sediment clusters,
313 changes in sediment imbrication, and temporal variability of local shear stress. As
314 well, the flow conditions at the bed load sampling point are unlikely to represent the
315 local conditions well in the place where the sediments were entrained, causing further
316 scatter in the relationship between the coarsest clast captured by the sampling basket
317 and the water stage at the site of monitoring.

318 The effective slope can be calculated by assuming a certain value of the critical
319 Shields parameter θ_{cr} unaffected by grain sorting, particle size interactions, channel
320 slope or high relative roughness. Although the critical Shields parameter can vary
321 locally, ranging from 0.03 to 0.09 (Buffington & Montgomery, 1997), if an
322 intermediate value of 0.05 is assumed, Eq. 13 provides a calculated value of i_e of 0.018
323 m/m. Interestingly, this value of effective slope is almost one order of magnitude
324 lower than the actual mean topographic channel slope ($i_b = 0.14$ m/m), revealing that
325 only a small part of the available bed shear stress is actually associated with sediment
326 transport during ordinary daily floods in the Estero Morales. This is well in agreement
327 with the high level of energy dissipation associated with bedforms (Chin & Wohl,
328 2005; Comiti et al., 2009), which can account for 80 % of the total flow resistance
329 (e.g. Canovaro et al., 2007; Chiari et al., 2010; Wilcox et al., 2011).

330 Our calculation of effective slope can be compared with the effective slope estimated
331 using the power-function relation proposed by Rickenmann and Recking (2011):

$$332 \quad \frac{i_e}{i_b} = (i_b^{-z} p)^e \quad (14)$$

333 where $p = 0.07$, $z = 0.47$ and $e = 1.2$ are calibrated using a large empirical dataset
334 (Chiari & Rickenmann, 2011; Rickenmann & Recking, 2011). For the Estero Morales,
335 Eqs. 13 and 14 provide an estimates of i_e/i_b , of around 0.13, remarkably similar to the
336 ratio resulting from the use of the value of i_e (0.018 m/m, see above), confirming that
337 the analysis based on competence is sound. Notably, Nitsche et al. (2011) combined
338 several bed load transport and flow resistance equations to account for flow energy
339 dissipation of step-pool morphology in steep streams. They recommended using the

340 slope decomposition approach (i.e., Rickenmann & Recking 2011) to increase the
 341 predictive power of bed load formulas that generally overestimate bed load transport
 342 in mountain streams by orders of magnitude (e.g. Vázquez-Tarrío & Menéndez-
 343 Duarte, 2015). Here we use effective slope to assess the increase in the predictive
 344 power of a widely-applied formula in a system with nearly unlimited sediment supply,
 345 and to derive the reference values needed for the later development of the present
 346 work. Specifically, we applied the Meyer-Peter & Muller equation (Meyer-Peter &
 347 Muller, 1948; Wong & Parker, 2006, hereafter MPM) using both the effective slope i_e
 348 and the topographical slope i_b , to calculate the value of the Shields parameter θ_{50} as:

$$349 \quad \theta_{50(i_e)} = \frac{h \cdot i_e}{\Delta \cdot D_{50}}; \theta_{50(i_b)} = \frac{h \cdot i_b}{\Delta \cdot D_{50}} \quad (15)$$

350 where h is the water depth measured in the field at the monitoring station and D_{50} is
 351 the median grain size. Figure 5 shows the typical daily fluctuation of θ_{50} over several
 352 days during the monitoring season, calculated with the effective slope i_e . The value of
 353 θ_{50} calculated with topographical slope would be one order of magnitude higher than
 354 shear stress, which is actually responsible for bed load transport. The outcome using
 355 topographical slope suggests that bed load even occurs at the lowest discharges at
 356 night. In contrast, effective slope provides values of shear stress ranging from 0.030 to
 357 0.075.

358 The shear stress calculated with Eq. 15 can be then applied to the revised MPM
 359 equation (Wong & Parker, 2006) to evaluate sediment transport rates. If applied to
 360 well sorted mixtures, the MPM reads as:

$$361 \quad q_s^{MPM} = 4(\theta - \theta_{cr})^{3/2} (g\Delta)^{1/2} D_{50}^{3/2} \quad (16)$$

362 where q_s^{MPM} represents calculated solid discharge per unit of active channel width. For
 363 poorly sorted mixtures, the unit solid discharge can be calculated for each grain size
 364 fraction D_i as follows:

$$365 \quad q_{si}^{MPM} = 4f_i(\theta - \xi_i\theta_{cr})^{3/2} (g\Delta)^{1/2} D_i^{3/2} \quad (17)$$

366 f_i being the volumetric frequency of each i^{th} grain size class and ξ_i the hiding factor
 367 calculated as $\xi_i = (D_i/D_{50})^{0.905}$, as previously suggested (Andrews, 1983; Parker et
 368 al., 1982). The instantaneous value of q_s^{MPM} is calculated using a value of the Shields
 369 stress obtained from Eq. (15), where the flow depth is provided by the local water

370 stage meter.

371 Figure 6 shows bed load rates measured using Bunte samplers *vs.* the dimensionless
372 shear stress calculated using the effective slope i_e . As expected, bed load rate increases
373 with shear stress, rising from $5 \times 10^{-8} \text{ m}^2 \text{ s}^{-1}$ at Shields of 0.03 to $5 \times 10^{-5} \text{ m}^2 \text{ s}^{-1}$ at Shields
374 of 0.06, and also the values of volumetric bed load rates are rather scattered. Figure 7
375 shows instead the values of bed load rates *vs.* the water stage at the time of sampling.
376 This graph allows plotting the MPM predictions calculated using both i_e and i_b
377 showing that using topographic slope to calculate MPM results in overestimating bed
378 load transport rates by more than one order of magnitude (Figure 7). Conversely,
379 MPM predictive power increases substantially when the effective slope is used,
380 especially at the higher transport rates.

381 Notably, the application of Rickenmann & Recking's approach (2011) closely
382 overlaps with the MPM formula based on i_e . This suggests that the use of effective
383 slope is a promising way to increase the predictive power of empirical bed load
384 formulas developed in flume experiments, in order to account for energy dissipation
385 due to morphological units, such as step-pools, which are usually associated with high
386 slope (Rickenmann & Recking, 2011). Indeed, the presence of step-pools produces a
387 large apparent increase in Shields stress (Chin & Wohl, 2005; Mao et al., 2008), and
388 can strongly affect bed load prediction (Recking et al., 2016).

389 It is worth stressing here that the reach-averaged shear stress calculated with Eq. 11 is
390 based on several assumptions (i.e. topographical slope is equal to the water slope and
391 to the energy slope) that are hardly met in steep streams like the Estero Morales (see
392 Yager et al., 2018). In future attempts, better estimates of effective slope and
393 predictions of bed load rates could be achieved by monitoring the slope of the water
394 surface or local flow velocity, or by using 2-D flow models to estimate the near-bed
395 shear stress (e.g. Monsalve et al, 2016).

396 The analysis also provides further insights into the transport regime of Estero Morales
397 during summer glacial-melting floods. As previously suggested (Capart & Fraccarollo,
398 2011; Berzi & Fraccarollo, 2013), the Shields value can discriminate between ordinary
399 (low Shields) and collisional (high Shields) bed load regimes for non-cohesive coarse
400 sediments in turbulent flows., Shields stress in the Estero Morales calculated using

401 effective slope is around 0.1, which suggests the occurrence of an ordinary bed load
402 transport regime in which sediment moves by sliding and saltation, with prolonged
403 rest periods, as was observed in the field. In contrast, the application of the
404 topographical slope i_b suggests an intense collisional regime in which particles also
405 frequently collide.

406

407 **5. Displacement lengths and virtual velocity of tracers**

408 As previously observed, finer particles in step-pools tend to undergo more
409 displacement than coarser particles (e.g. Church and Hassan, 1992). Figure 8 shows
410 the plotted measured total displacement lengths of single tracers scaled by the mean
411 total displacement of the median grain size ($\ell_{50-surf}$) as a function of the ratio
412 between tracer size (D) and the median subsurface grain size (D_{50-sub}). The average
413 value of dimensionless flight distance for binned classes of dimensionless particles
414 sizes decreases for coarser sediments. Although considerable scatter is observed, the
415 size-dependent trend is confirmed and the field data are plotted around previously
416 derived empirical formulas (i.e. Church & Hassan, 1992; Vasquez-Tarrio et al., 2019).
417 However, the empirical relationship is not statistically significant ($R^2=0.095$; Figure
418 8).

419 Virtual velocity is usually calculated as the ratio between the displacement length and
420 the time between the survey when the tracers were placed in the field and the one
421 when they were retrieved. Because the daily fluctuations in discharges in the Estero
422 Morales are fairly regular in summer (see Figure 5), we consider here that daily
423 hydrographs are only characterized by over threshold flows 30% of the time ($\theta_{50} >$
424 θ_{cr}). Following this logic, we calculated the average virtual velocity of each PIT tracer
425 using their travelled distance and 30% of the time interval between the two subsequent
426 surveys, irrespective of the survey date.

427 The virtual velocity of particles of different sizes can be used to quantify the
428 volumetric bed load transport rates using Eq. 6, which mainly requires virtual velocity
429 and the thickness of the active layer δ . The thickness of the active sediment layer
430 generally depends on local hydraulic conditions and bed texture (e.g., Houbrechts et
431 al., 2012). Although δ depends on the shear stress acting locally (Wilson, 1987;

432 Kumbhakar et al., 2018; Brenna et al., 2019), it can be reasonably assumed that the
 433 thickness of the active layer is proportional to the surface grain size $\delta = a D_{50}$
 434 (Haschenburger & Church, 1998) with a ranging from 1 to 3 (Hassan & Bradley,
 435 2017). Einstein (1950) originally estimated a as twice the surface grain size. As a first
 436 approximation in this paper, we assume that the thickness of the active layer is equal
 437 to the median surface grain size. This is reasonable during the ordinary fluctuations of
 438 discharge monitored in 2014 and 2015, as only a few tracers were found buried during
 439 the surveys. Given that the step-pool remained stable over the two years of
 440 observations, this indicates that only minor vertical adjustments occurred in the
 441 channel bed. Arguably, the assumption that $\delta = D_{50}$ would not hold true for higher-
 442 magnitude events that affect the stability of step-pools sequences, as the thickness of
 443 the active layer would become larger and affected by erosion/deposition dynamics.
 444 The above considerations on how to evaluate the virtual velocity and the active layer
 445 in the field are useful in considering Eq. 7.

446 If bed load transport rates q_{si} are calculated using the MPM formula based on the
 447 effective slope (Eq. 17; Figure 7), Eqs. 7 and 17 are combined to obtain V_{vi} in m/day:

$$448 \quad V_{vi} = \frac{1}{0.3 D_{50}} \int_{1day} q_{si}^{MPM} dt \quad (18)$$

449 Here we assume a value of c_b equal to 1, and a grain size distribution range
 450 corresponding to that of the PIT population, thus underrepresenting the finer fractions,
 451 to some extent. In Eq. 18 V_{vi} represents the virtual velocity (m/day) averaged over the
 452 portion of the day when $\theta_{50} > \theta_{cr}$. The two sides of Eq. 18 are plotted against grain size
 453 in Figure 9. As documented elsewhere (e.g. Liebault et al., 2012), despite the high
 454 degree of scatter, virtual velocities tend to decrease hyperbolically with grain size.
 455 This behavior is reproduced fairly well by the MPM volumes calculated when the
 456 hiding effect (see Eq. 17) and effective slope are considered. Interestingly, using
 457 topographical rather than effective slope in the calculation of bed load transport rates
 458 would result in a major overestimation of virtual velocity, especially of the coarser
 459 fractions, consistently with results in Figure 7. The overall reduction of virtual
 460 velocities with grain size indicates that the shear stress exerted by the flow over the
 461 bed during a daily flood is never high enough to make the size of transported sediment
 462 independent of critical Shields stress (e.g. the transport is size-selective), and confirms

463 that the sediment transport regime belongs to the ordinary bed load mode.
464 The tracer data show virtual velocities of up to 65 m per day (looking at the binned
465 data in Figure 9) and null values for grain size coarser than 250 mm. These values are
466 representative of the flow conditions obtained by restricting the analysis to intraday
467 sub-periods characterized by $\theta > \theta_{cr}$ (see Figure 5). Clearly, if averaged over an entire
468 day, including periods at $\theta < \theta_{cr}$, when no bed load transport occurs, we would obtain
469 lower virtual velocity.

470

471 **6. The statistics of sediment resting times and Einstein conjecture**

472 Ordinary tracer studies focus on the mobility and virtual velocity of sediments during
473 floods. Frequent subsequent surveys with the mobile antenna, combined with the
474 natural daily fluctuations in discharge, allowed us to focus on the tracers that remained
475 in the same location over two or more surveys in order to calculate sediment resting
476 times. The field surveys conducted over consecutive days allowed for directly
477 measuring the resting times T_i of the PIT tags of different grain sizes. When a tracer
478 was recovered in the same position in the following survey, the resting time was
479 calculated, representing the time interval elapsing from the first to last retrieval in the
480 same position. Using these direct measurements, the mean resting time obtained by
481 averaging all the PITs is approximately 8.6 days. If the resting times are calculated
482 using the portion of the day when $\theta > \theta_{cr}$ (which represents approximately 30% of the
483 time, see Figure 5), the mean resting time drops to around 2.6 days of continuous over-
484 threshold flow with active bed load transport. Figure 10 reports the values of these
485 directly measured resting times (red dots) as a function of tracer size. The lack of data
486 points for durations of less than 8 hours (30% of a day, when $\theta > \theta_{cr}$) is related to the
487 temporal resolution of field surveys (i.e., at least one day apart from each other),
488 which is an intrinsic limitation of non-continuous tracking. Interestingly, the resting
489 times are not sensitive ($R^2 = 0.03$) to the grain size of tracers, indicating that the
490 probability of a grain in the Estero Morales being entrained is independent of its size
491 (Figure 10).

492 Figure 10 also shows a series of resting times calculated indirectly, derived from a re-
493 evaluation of the Einstein approach along with the empirical resting times derived

494 from repeated field surveys. The method used to calculate this dataset is explained
495 below.

496 We took advantage of the fact that any measured PIT displacement is the cumulative
497 distance travelled over a known inter-survey time interval, without taking into account
498 that particles tend to move on subsequent jumps that include multiple stops with
499 relative resting times. Conceptually, at least one resting time is associated with any
500 single flight (i.e., a distance > 0) that took place during an inter-survey interval. We
501 developed a method to work with these data and extract one or more resting time from
502 any inter-survey displacement. In Einstein's (1950) bed load formula (Eq. 2), the flight
503 distance \bar{L}_i is assumed to depend on the size of the sediment D_i and on ω , a positive
504 dimensionless constant ($\omega \approx 100$):

$$505 \quad \bar{L}_i = \omega D_i \quad (19)$$

506 Given that \bar{L}_i depends only on D_i (see Eq. 19), in Einstein formula (Eq. 1) the bed
507 load intensity depends completely on the other predictor E_i representing the number of
508 particles entrained per unit time and unit bed-surface area. In order to interpret our
509 dataset, we relaxed the Einstein constraint and adopted the following linear
510 relationship:

$$511 \quad \bar{L}_i = \omega D_i + c \quad (20)$$

512 The constant c makes it possible, at least theoretically, to obtain a negative value of the
513 coefficient ω , which is always positive in experimental studies (Campagnol et al.,
514 2012). The presence of c also implies that there are parts of the bed surface occupied
515 by stable bed-form structures over which particles do not stop during ordinary events
516 (i.e., floods are not able to destroy bed forms). As in Einstein (1950), Eq. 20 assumes
517 that the coefficients are constant and independent of both grain size and bed load
518 intensity.

519 By applying a recursive procedure, we obtain L_i and a rich sample of resting times that
520 together contribute to describing the distribution of the directly measured resting
521 times. In the first iteration of the procedure, which started with guess values of ω and c
522 (e.g., the Einstein's values, $\omega = 100$, $c = 0$ m), and we used Eq. 20 to calculate L_i for
523 all grain sizes. Each measured inter-survey displacement was divided by L_i to obtain
524 the number of resting periods the particle underwent during such displacement. The

525 inter-survey time interval was thus divided by the number of resting periods to
526 calculate the duration of each one. These additional and indirect values enrich the
527 statistics of the resting times, summing to those directly measured in the field.
528 All the values of resting times, either directly measured and inferred from the
529 displacements, were used to calculate a mean value \bar{T} . We then used the measured
530 average values of virtual velocity for each grain size (see Figure 9) to indirectly obtain
531 the average flight distance L_i based on the grain size. This is accomplished by
532 multiplying the virtual velocity, which depends on the grain size (we used the binned
533 values reported in Figure 9), by \bar{T} . Based on these values of L_i , the parameters ω and c
534 were back-calculated, using Eq. 20, and iterations were repeated until the values of ω
535 and c remained constant.

536 Figures 10 and 11 illustrate the results obtained at the end of the direct and indirect
537 approaches of the calculation. Neither directly measured data (red dots in Figure 10)
538 nor the indirect data extracted from displacements (blue dots in Figure 10) show
539 significant dependence of resting times on grain size. Figure 11 shows the statistical
540 distribution of resting times of the two datasets. The directly measured resting times
541 displays a shapeless probability-density distribution (Figure 11) which becomes much
542 more outlined when measured and displacement-inferred resting times are merged
543 (Figure 11b). Their overall mean is about 32 hours (1.35 days). The directly measured
544 and the displacement-inferred resting times concur when below-threshold periods (i.e.
545 when the Shields value is below the critical level) have been removed. Because θ
546 exceeds θ_{cr} for approximately 30% of the time, an effective mean period T_r of 32 hours
547 represents on average 4.5 days in the monitored reach of Estero Morales. Figure 11
548 clearly indicates that the inequality reported in Eq. 3 fully applies, as the probability
549 density distribution of the resting times are far from being uniform.

550 Our results further show that the relation between L_i and D_i does not confirm Einstein's
551 assumption that $\omega = 100$ and $c = 0$ m. Indeed, the flight distance of single grains
552 decreases with particle size, and we obtained values of ω and c of -200 [-] and 50 m,
553 respectively (Figure 12). Interestingly, ω is negative, revealing that in a naturally
554 structured step-pool channel experiment, sediment mobility is completely different
555 from that in flume runs with well sorted sediments and no bedforms (Campagnol et al.,

556 2012; Lajeunesse et al., 2010; Lee et al., 2006; Radice et al., 2013; Fraccarollo &
557 Hassan, 2019). Deviations from Einstein conjecture were reported by Habersack
558 (2001) in one of the first reports on step lengths and rest periods using tracers in the
559 field.

560 It is worth discussing the reason ω has a negative value. Once small particles are
561 dislodged, they are transported for long distances, before coming to rest. This is
562 consistent with what is shown in Figure 10 and with the outcomes of recent works
563 (e.g., Vázquez-Tarrío et al., 2019). The value obtained for c is higher than the average
564 distance between steps in Estero Morales, which is around 10 m. The spacing between
565 pools is a relevant geomorphic dimension of step-pool sequences, given that it is
566 closely related to step formation (Curran, 2007) and flow resistance (Giménez-Curto
567 & Corniero, 2006). During a given ordinary glacier-melting induced flood, the tracer
568 displacements are influenced by the bed morphology and selected according to the
569 grain size. Pools are particularly difficult to pass, and it is where coarse particles are
570 more likely found. The work by Habersack (2001) is one of the few to have dealt with
571 Einstein predictors using field data. This author radio-tracked gravel particles in a
572 large braided river and gathered hundreds of direct measurements of resting times and
573 flight distances. Interestingly, although working in a different bed form setting (i.e.,
574 dunes, gravel sheets and bars), Habersack (2001) also found a negative relationship
575 between the dimensionless step lengths L_i/D_{50} and scaled particle size (D_i/D_{50}).

576 Through flume experiments, Pyrce and Ashmore (2003) showed that the distribution
577 of mean flight length is related to pool-bar spacing and that only a small proportion of
578 particles are able to move beyond the first bar downstream from the entrainment site.
579 Present and previous results confirm the dependence of grain flights on morphological
580 features, in particular the control that bed forms can exert on coarse particles,
581 preventing long flights, which support the need for a negative value for the
582 proportionality parameter ω in our generalization of the Einstein relation (Eq. 20).

583 It is worth stressing that all results presented here derive from field measurement
584 conducted during ordinary daily floods generated by the glacial melt. Larger events
585 (i.e. intense rainfall events in early autumns in the case of the Estero Morales) would
586 result in disruption of the step-pool morphology, deeper sediment active layer, and

587 large erosion/deposition processes in the channel and banks. Under these conditions,
588 the statistical features of sediment displacement lengths and resting times would be
589 likely quite different, and the very premise of the present analysis, i.e. the
590 decomposition of the topographic slope, would be affected. It would be interesting to
591 corroborate the Einstein's contention under higher magnitude events in the Estero
592 Morales when, as in laboratory flume experiments, most of the bed would be mobile.

593

594 **7. Conclusions**

595 In this work, we presented and analyzed a new dataset collected over two years of
596 sediment transport monitoring, including PIT-tracer displacements and direct
597 volumetric sampling with Bunte traps, in Estero Morales (Chile). The latter data
598 allowed us to assess the effective slope of the study reach, at least for ordinary floods,
599 and to apply the relation proposed by Meyer-Peter and Müller to successfully predict
600 sediment discharge. This physically based method of breaking down the total (or
601 geometric) slope yielded results that are in good agreement with previous formulations
602 and can be tested straightforwardly in other streams, provided a meter gauge is
603 installed in the reach and volumetric samples of bed load are taken in a range of
604 discharges. We further presented the link between Einstein's predictors and virtual
605 velocity. Frequent tracking of tracer positions, along with the regularity of daily floods
606 in Estero Morales, allowed us to collect a first sample of resting times. Then, by
607 adopting a generalized version of Einstein's fundamental law, we inferred additional
608 resting times and flight distances from inter-survey data of tracer displacements. Our
609 results contradict Einstein's assumption and show a surprising decrease in flight
610 distances with larger grain sizes, as opposed to a linear increase. This finding is
611 conceptually consistent with the notion that bed macroroughness, which is responsible
612 for slope decomposition, plays a prominent role in processes that characterize
613 sediment transport, like entrainment and deposition. We also observed that resting
614 times do not depend significantly on tracer size.

615

616 **Acknowledgments**

617 This work was supported by the project Fondecyt Regular 1170657. We thank Joaquin

618 Lobato, Juan Pablo del Pedregal, Enzo Montenegro, Paolo Bertoncetto and Riccardo
619 Rainato for their help in the field. We are grateful to the Chilean National Park Service
620 (CONAF) for providing access to the sample locations and on-site support of our
621 research. Two anonymous reviewers, John Laronne, and the Associated Editor Luca
622 Solari are thanked for providing several constructive commentaries on a first version
623 of the manuscript. The data from field measurements is available for download in an
624 online open data repository (DOI: 10.5281/zenodo.3274762).

625

626 **FIGURE CAPTION**

627 **Figure 1.** Location and map of the Estero Morales basin.

628 **Figure 2.** Views of the Estero Morales (a) at the monitored cross-section; (b) at the
629 upstream end of the reach where the PIT tracers were placed and surveyed; (c) during
630 a PIT survey conducted with a portable antenna; and (d) during bed load sampling
631 using Bunte traps. The channel width is about 7 m.

632 **Figure 3.** Surface and sub-surface grain size distribution in the monitored reach of the
633 Estero Morales, and size distribution of PIT tracers.

634 **Figure 4.** Relationship between the coarsest clast (D_{100}) collected with the Bunte
635 sampler and the water depth at the time of sampling, as measured at the monitoring
636 site during events recorded in 2014 and 2015). The filled black dots represent the
637 average values of D_{100} for binned classes of water depth. The regression plots as D_{100}
638 $= 0.2436h - 0.0056$ ($R^2 = 0.29$).

639 **Figure 5.** Temporal trend of the dimensionless shear stress over three exemplary
640 weeks of January 2014 in the Estero Morales calculated with Eq. 15 using the
641 effective slope i_e . The horizontal line refers to the assumed critical value of shear
642 stress ($\theta_{50(i_e)} = 0.05$), which corresponds to a value of Shields of almost 0.40 if
643 calculated using the topographical slope i_b .

644 **Figure 6.** Bed load transport rates as measured with the Bunte traps in 2014 and 2015,
645 plotted against the Shields parameter calculated using the effective slope. The filled
646 black dots represent the average values of q_s for binned classes of shear stress.

647 **Figure 7.** Bed load transport rates plotted against the water depth water depth at the
648 time of sampling. The filled black dots represent the average values of q_s for binned

649 classes of water depths. The figure shows that the Meyer-Peter Mueller equation
650 predicts the order of magnitude of bed load rates if the Shield stress is calculated using
651 i_e , but overestimates actual transport rates by more than two orders of magnitude if
652 calculated using i_b .

653 **Figure 8.** Dimensionless displacement ℓ_* of individual particles (scaled by the
654 averaged travel distance of particles similar to the surface size D_{50}) as a function of
655 dimensionless particle size D^* (scaled by the subsurface median size). The best fit
656 regression is $\ell_* = -0.296 D_* + 2.389$ ($n=517$; $P<0.001$; $R^2=0.095$). The filled dots
657 represent the average values of dimensionless displacements for binned classes of
658 dimensionless particles sizes. Empirical equations of Church & Hassan (1992) and
659 Vasquez-Tarrio et al. (2019) are plotted as well.

660 **Figure 9.** Virtual velocities plotted against the size of tracers used in the Estero
661 Morales. The filled dots represent the average values of virtual velocity for binned
662 classes of particles sizes. The solid line represents Eq. 17.

663 **Figure 10.** Resting times of coarse particles directly measured or computed through
664 displacement surveys of PIT tags.

665 **Figure 11.** Histograms of the rest periods from direct surveys (left panel), and all rest
666 periods including those calculated through displacement surveys (right panel).

667 **Figure 12.** Experimental data of flight displacement versus grain size, including the
668 best fit of Eq. 20. Einstein's line represents $L_o = 100D_i$. The empirical equation of
669 Habersack (2001), applied using D_{50} of the Estero Morales is plotted as well.

670

671 REFERENCES

- 672 Andrews, E. D. (1983). Entrainment of gravel from naturally sorted riverbed material.
673 *Geological Society of America Bulletin*, 94, 1225-1231.
- 674 Badoux, A., Andres, N., and Turowski, J. M. (2014). Damage costs due to bedload
675 transport processes in Switzerland. *Natural Hazards and Earth System Science*,
676 14, 279-294. <https://doi.org/10.5194/nhess-14-279-2014>.
- 677 Batalla, R. J., & Martín-Vide, J. P. (2001). Thresholds of particle entrainment in a
678 poorly sorted sandy gravel-bed river. *Catena*, 44(3), 223–243.
679 [http://doi.org/10.1016/S0341-8162\(00\)00157-0](http://doi.org/10.1016/S0341-8162(00)00157-0)
- 680 Berzi, D., & Fraccarollo, L. (2013). Inclined, collisional sediment transport. *Physics of*
681 *Fluids*. <http://doi.org/10.1063/1.4823857>
- 682 Bradley, D. N., Tucker, G. E., & Benson, D. A. (2010). Fractional dispersion in a sand
683 bed river. *Journal of Geophysical Research: Earth Surface*, 115(F1).

- 684 Brardinoni, F., & Hassan, M. A. (2007). Glacially induced organization of channel-
685 reach morphology in mountain streams. *Journal of Geophysical Research:*
686 *Earth Surface*, 112(F3).
- 687 Brenna, A., Surian, N., & Mao, L. (2019). Virtual Velocity Approach for Estimating
688 Bed Material Transport in Gravel-Bed Rivers: Key Factors and Significance.
689 *Water Resources Research*, 55(2), 1651–1674.
- 690 Buffington, J. M., & Montgomery, D. R. (1997). A systematic analysis of eight
691 decades of incipient motion studies, with special reference to gravel-bedded
692 rivers. *Water Resources Research*, 33(8), 1993–2029.
693 <http://doi.org/10.1029/96WR03190>
- 694 Bunte, K., Abt, S. R., Potyondy, J. P., & Ryan, S. E. (2004). Measurement of coarse
695 gravel and cobble transport using portable bedload traps. *Journal of Hydraulic*
696 *Engineering*, 130(9), 879–893. [http://doi.org/10.1061/\(ASCE\)0733-9429\(2004\)](http://doi.org/10.1061/(ASCE)0733-9429(2004)130(9)879)
- 697 Campagnol, J., Radice, A., & Ballio, F. (2012). Scale-based statistical analysis of
698 sediment fluxes. *Acta Geophysica*. <http://doi.org/10.2478/s11600-012-0028-6>
- 699 Canovaro, F., Paris E., Solari L. (2007). Effects of macro-scale bed roughness
700 geometry on flow resistance. *Water Resources Research*, 43, W10414,
701 [doi:10.1029/2006WR005727](https://doi.org/10.1029/2006WR005727).
- 702 Capart, H., & Fraccarollo, L. (2011). Transport layer structure in intense bed-load.
703 *Geophysical Research Letters*. <http://doi.org/10.1029/2011GL049408>
- 704 Chapuis, M., Bright, C. J., Hufnagel, J., & Macvicar, B. (2014). Detection ranges and
705 uncertainty of passive Radio Frequency Identification (RFID) transponders for
706 sediment tracking in gravel rivers and coastal environments. *Earth Surface*
707 *Processes and Landforms*, 39(15), 2109–2120. <http://doi.org/10.1002/esp.3620>
- 708 Chiari, M., & Rickenmann, D. (2011). Back-calculation of bedload transport in steep
709 channels with a numerical model. *Earth Surface Processes and Landforms*.
710 <http://doi.org/10.1002/esp.2108>
- 711 Chiari, M., Friedl, K., & Rickenmann, D. (2010). A one-dimensional bedload transport
712 model for steep slopes. *Journal of Hydraulic Research*.
713 <http://doi.org/10.1080/00221681003704087>
- 714 Chin, A., & Wohl, E. (2005). Toward a theory for step pools in stream channels.
715 *Progress in Physical Geography*, 29(3), 275–296.
- 716 Church M., Hassan M.A. (1992). Size and distance of travel of unconstrained clasts on
717 a streambed. *Water Resources Research*, 28, 299-303.
- 718 Church, M. (2006). Bed Material Transport and the Morphology of Alluvial River
719 Channels. *Annual Review of Earth and Planetary Sciences*, 34(1), 325–354.
720 <http://doi.org/10.1146/annurev.earth.33.092203.122721>
- 721 Church, M., & Zimmermann, A. (2007). Form and stability of step-pool channels:
722 Research progress. *Water Resources Research*, 43(3).
723 <http://doi.org/10.1029/2006WR005037>
- 724 Comiti, F., & Mao, L. (2012). Recent Advances in the Dynamics of Steep Channels.
725 In M. Church, P. M. Biron, & A. G. Roy (Eds.), *Gravel-Bed Rivers: Processes,*
726 *Tools, Environments*. Chichester, UK: John Wiley & Sons, Ltd.
- 727 Comiti, F., Cadol, D., & Wohl, E. (2009). Flow regimes, bed morphology, and flow
728 resistance in self-formed step-pool channels. *Water Resources Research*.
729 <http://doi.org/10.1029/2008WR007259>

- 730 Curran, J. C. (2007). Step-pool formation models and associated step spacing. *Earth*
731 *Surface Processes and Landforms*, 32(11), 1611–1627.
732 <http://doi.org/10.1002/esp.1589>
- 733 Dell’Agnese, A., Brardinoni, F., Toro, M., Mao, L., Engel, M., & Comiti, F. (2015).
734 Bedload transport in a formerly glaciated mountain catchment constrained by
735 particle tracking. *Earth Surface Dynamics*, 3(4), 527–542.
736 <http://doi.org/10.5194/esurf-3-527-2015>
- 737 Dell’Agnese, A., Mao, L., & Comiti, F. (2014). Calibration of an acoustic pipe sensor
738 through bedload traps in a glacierized basin. *Catena*, 121, 222–231.
- 739 Einstein, H. A. (1950). *The Bed-Load Function for Sediment Transportation in Open*
740 *Channel Flows*. Soil Conservation Service, no. 1026.
- 741 Escauriaza, C., Paola, C., & Voller, V. R. (2017). Computational models of flow,
742 sediment transport and morphodynamics in rivers. In *Gravel-Bed Rivers:*
743 *Process and Disasters* (pp. 1–31). <http://doi.org/10.1002/9781118971437.ch1>
- 744 Ferguson, R. (2007). Flow resistance equations for gravel- and boulder-bed streams.
745 *Water Resources Research*. <http://doi.org/10.1029/2006WR005422>
- 746 Fraccarollo, L., & Hassan, M. A. (2019). Einstein conjecture and resting-time statistics
747 in the bed-load transport of monodispersed particles. *Journal of Fluid*
748 *Mechanics*, 876, 1077-1089.
- 749 Giménez-Curto, L. A., & Corniero, M. A. (2006). Comment on “Characteristic
750 dimensions of the step-pool bed configuration: An experimental study” by
751 Joanna C. Curran and Peter R. Wilcock. *Water Resources Research*, 42(3), 6–
752 8. <http://doi.org/10.1029/2005WR004296>
- 753 Green, K. C., Brardinoni, F., & Alila, Y. (2013). Channel morphology and bed-load
754 yield in fluvial, formerly-glaciated headwater streams of the Columbia
755 Mountains, Canada. *Geomorphology*, 188, 96–109.
- 756 Green, K., Alila, Y., & Brardinoni, F. (2015). Patterns of bedload entrainment and
757 transport in forested headwater streams of the Columbia Mountains, Canada.
758 *Earth Surface Processes and Landforms*, 40(4), 427–446.
- 759 Habersack, H. M. (2001). Radio-tracking gravel particles in a large braided river in
760 New Zealand: A field test of the stochastic theory of bed load transport
761 proposed by Einstein. *Hydrological Processes*, 15(3), 377–391.
- 762 Haschenburger, J. K., & Church, M. (1998). Bed material transport estimated from the
763 virtual velocity of sediment. *Earth Surface Processes and Landforms*, 23(9),
764 791–808. [http://doi.org/10.1002/\(SICI\)1096-9837\(199809\)23:9<791::AID-
765 ESP888>3.0.CO;2-X](http://doi.org/10.1002/(SICI)1096-9837(199809)23:9<791::AID-ESP888>3.0.CO;2-X)
- 766 Hassan, M.A., Bradley, D. N. (2017). Geomorphic controls on tracer particle
767 dispersion in gravel bed rivers. In *Gravel-Bed Rivers: Process and Disasters*
768 (ed. Tsutsumi, D. & Laronne, J. B.), chap. 6, pp. 159–184. Wiley-Blackwell.
- 769 Hassan, M. A., Voepel, H., Schumer, R., Parker, G., & Fraccarollo, L. (2013).
770 Displacement characteristics of coarse fluvial bed sediment. *Journal of*
771 *Geophysical Research: Earth Surface*, 118 (February 2012), 1–11.
772 <http://doi.org/10.1029/2012JF002374>
- 773 Hohermuth, B., & Weitbrecht, V. (2018). Influence of Bed-Load Transport on Flow
774 Resistance of Step-Pool Channels. *Water Resources Research*, 54(8), 5567–
775 5583. <http://doi.org/10.1029/2017WR021523>

- 776 Houbrechts, G., Van Campenhout, J., Levecq, Y., Hallot, E., Peeters, A., & Petit, F.
777 (2012). Comparison of methods for quantifying active layer dynamics and
778 bedload discharge in armoured gravel-bed rivers. *Earth Surface Processes and*
779 *Landforms*, 37(14), 1501–1517. <http://doi.org/10.1002/esp.3258>
- 780 Kumbhakar, M., Kundu, S., Ghoshal, K. (2018). An explicit analytical expression for
781 bed-load layer thickness based on maximum entropy principle. *Physics Letters*
782 *A*, 382(34), 2297-2304.
- 783 Lajeunesse, E., Malverti, L., & Charru, F. (2010). Bed load transport in turbulent flow
784 at the grain scale: Experiments and modeling. *Journal of Geophysical*
785 *Research: Earth Surface*. <http://doi.org/10.1029/2009JF001628>
- 786 Lamb, M. P., Dietrich, W. E., & Venditti, J. G. (2008). Is the critical shields stress for
787 incipient sediment motion dependent on channel-bed slope? *Journal of*
788 *Geophysical Research: Earth Surface*, 113(2), 1–20.
789 <http://doi.org/10.1029/2007JF000831>
- 790 Laronne, J.B., Garcia, C. & Reid, I. (200)1. Mobility of patch sediment in gravel bed
791 streams: patch character and its implications for bedload. In M. Paul Mosley
792 (editor), *Gravel-Bed Rivers V*, New Zealand Hydrological Society Inc.,
793 Wellington, New Zealand, pp. 249-289.
- 794 Lee, H. Y., Lin, Y. T., You, J. Y., & Wang, H. W. (2006). On three-dimensional
795 continuous saltating process of sediment particles near the channel bed.
796 *Journal of Hydraulic Research*.
797 <http://doi.org/10.1080/00221686.2006.9521689>
- 798 Lenzi MA, Mao L, Comiti F. (2004). Magnitude–frequency analysis of bed load data
799 in an alpine boulder bed stream. *Water Resources Research*, 40, W07201. DOI:
800 10.1029/2003WR002961.
- 801 Lenzi MA, Mao L, Comiti F. (2006). When does bedload transport begin in steep
802 boulder-bed streams? *Hydrological Processes*, 20, 3517-3533.
- 803 Liébault, F., Laronne, J.B. (2008). Evaluation of bedload yield in gravel-bed rivers
804 using scour chains and painted tracers: the case of the Esconavette Torrent
805 (Southern French Prealps). *Geodinamica Acta*, 21(1-2), 23-34. DOI:
806 10.3166/ga.21.23-34.
- 807 Liébault, F., Bellot, H., Chapuis, M., Klotz, S., & Deschâtres, M. (2012). Bedload
808 tracing in a high-sediment-load mountain stream. *Earth Surface Processes and*
809 *Landforms*. <http://doi.org/10.1002/esp.2245>
- 810 Magirl, C.S., Hilldale, R.C., Curran, C.A., Duda, J.J., Straub, T.D., Domanski, M.,
811 Foreman, J.R. (2015). Large-scale dam removal on the Elwha River,
812 Washington, USA: Fluvial sediment load. *Geomorphology*, 246, 669-686.
813 <https://doi.org/10.1016/j.geomorph.2014.12.032>.
- 814 Maniatis G., Hoey T.B., Hassan M.A., Sventek J., Hodge R., Drysdale T., & Valyrakis
815 M., (2017). Calculating the explicit probability of entrainment based on
816 inertial acceleration measurements. *Journal of Hydraulic Engineering* 143,
817 04016097.
- 818 Mao, L., & Carrillo, R. (2017). Temporal dynamics of suspended sediment transport in
819 a glacierized Andean basin. *Geomorphology*, 287.
820 <http://doi.org/10.1016/j.geomorph.2016.02.003>

821 Mao, L., Carrillo, R., Escauriaza, C., & Iroume, A. (2016). Flume and field-based
822 calibration of surrogate sensors for monitoring bedload transport.
823 *Geomorphology*, 253, 10–21. <http://doi.org/10.1016/j.geomorph.2015.10.002>
824 Mao, L., Dell’Agnese, A., & Comiti, F., 2017. Sediment motion and velocity in a
825 glacier-fed stream. *Geomorphology*, 291, 69–79.
826 Mao, L., Uyttendaele, G. P., Iroumé, A., & Lenzi, M. A. (2008). Field based analysis
827 of sediment entrainment in two high gradient streams located in Alpine and
828 Andine environments. *Geomorphology*, 93(3–4), 368–383.
829 <http://doi.org/10.1016/j.geomorph.2007.03.008>
830 Masteller, C. C., Finnegan, N. J., Turowski, J. M., Yager, E. M., & Rickenmann, D.
831 (2019). History-dependent threshold for motion revealed by continuous
832 bedload transport measurements in a steep mountain stream. *Geophysical*
833 *Research Letters*, 46, 2583–2591.
834 Meyer-Peter, E., & Muller, R. (1948). Formulas for bed-load transport. In *2nd Meeting*
835 *of the International Association on Hydraulic Structures Research*.
836 <http://doi.org/1948-06-07>
837 Monsalve, A., Yager, E. M., Turowski, J. M., & Rickenmann, D. (2016). A
838 probabilistic formulation of bed load transport to include spatial variability of
839 flow and surface grain size distributions. *Water Resources Research*, 52, 3579–
840 3598. doi:10.1002/2015WR017694.
841 Monsalve, A., Yager, E. M., & Schmeeckle, M. W. (2017). Effects of Bed Forms and
842 Large Protruding Grains on Near-Bed Flow Hydraulics in Low Relative
843 Submergence Conditions. *Journal of Geophysical Research: Earth Surface*,
844 122(10), 1845–1866. <http://doi.org/10.1002/2016JF004152>
845 Nikora, V., Habersack, H., Huber, T., & McEwan, I. (2002). On bed particle diffusion
846 in gravel bed flows under weak bed load transport. *Water Resources Research*,
847 38(6), 11–17.
848 Nitsche, M., D. Rickenmann, J. M. Turowski, A. Badoux, and J. W. Kirchner (2011).
849 Evaluation of bedload transport predictions using flow resistance equations to
850 account for macro-roughness in steep mountain streams. *Water Resources*
851 *Research*, 47, W08513, doi:10.1029/2011WR010645.
852 Parker, G., Klingeman, P. C., & McLean, D. G. D. (1982). Bedload and Size
853 Distribution in Paved Gravel-Bed Streams. *J. Hydraul. Div. Am. Soc. Civ. Eng.*
854 [http://doi.org/10.1061/\(ASCE\)0733-9429\(1983\)109:5\(793\)](http://doi.org/10.1061/(ASCE)0733-9429(1983)109:5(793))
855 Pyrce, R. S., & Ashmore, P. E. (2003). Particle path length distributions in meandering
856 gravel-bed streams: Results from physical models. *Earth Surface Processes*
857 *and Landforms*, 28(9), 951–966.
858 Phillips, C.B., Martin, R.L., & Jerolmack, D.J. (2013). Impulse framework for
859 unsteady flows reveals superdiffusive bedload transport. *Geophysical Research*
860 *Letters*, 40, 1328–1333.
861 Radice, A., Nikora, V., Campagnol, J., & Ballio, F. (2013). Active interactions
862 between turbulence and bed load: Conceptual picture and experimental
863 evidence. *Water Resources Research*. <http://doi.org/10.1029/2012WR012255>
864 Recking, A., Piton, G., Vazquez-Tarrio, D., & Parker, G. (2016). Quantifying the
865 Morphological Print of Bedload Transport. *Earth Surface Processes and*
866 *Landforms*, 41(6), 809–822. <http://doi.org/10.1002/esp.3869>





- 867 Rickenmann, D., & Recking, A. (2011). Evaluation of flow resistance in gravel-bed
868 rivers through a large field data set. *Water Resources Research*.
869 <http://doi.org/10.1029/2010WR009793>
- 870 Saletti, M., Molnar, P., Hassan, M. A., & Burlando, P. (2016). A reduced-complexity
871 model for sediment transport and step-pool morphology. *Earth Surface*
872 *Dynamics*, 4(3), 549–566. <http://doi.org/10.5194/esurf-4-549-2016>
- 873 Schneider, J. M., Rickenmann, D., Turowski, J. M., Schmid, B., & Kirchner, J. W.
874 (2016). Bed load transport in a very steep mountain stream (Riedbach,
875 Switzerland): Measurement and prediction. *Water Resources Research*, 52(12),
876 9522–9541.
- 877 Shih, W., & Diplas, P. (2018). A unified approach to bed load transport description
878 over a wide range of flow conditions via the use of conditional data treatment.
879 *Water Resources Research*, 54(5), 3490–3509.
- 880 Singh, A., Fienberg, K., Jerolmack, D. J., Marr, J., & Fofoula-Georgiou, E. (2009).
881 Experimental evidence for statistical scaling and intermittency in sediment
882 transport rates. *Journal of Geophysical Research: Earth Surface*.
883 <http://doi.org/10.1029/2007JF000963>
- 884 Turowski, J. M., E. M. Yager, A. Badoux, D. Rickenmann, and P. Molnar (2009). The
885 impact of exceptional events on erosion, bedload transport and channel
886 stability in a step-pool channel. *Earth Surface Processes and Landforms*, 34,
887 1661-1673.
- 888 Vázquez-Tarrio, D., & Menéndez-Duarte, R. (2015). Assessment of bedload equations
889 using data obtained with tracers in two coarse-bed mountain streams (Narcea
890 River basin, NW Spain). *Geomorphology*, 238, 78–93.
- 891 Vázquez-Tarrio, D., Recking, A., Liébault, F., Tal, M., & Menéndez-Duarte, R.
892 (2019). Particle transport in gravel-bed rivers: Revisiting passive tracer data.
893 *Earth Surface Processes and Landforms*, 44(1), 112–128.
894 <http://doi.org/10.1002/esp.4484>
- 895 Vericat, D., Church, M., & Batalla, R. J. (2006). Bed load bias: Comparison of
896 measurements obtained using two (76 and 152 mm) Helley-Smith samplers in
897 a gravel bed river. *Water Resources Research*, 42(1), 1–13.
898 <http://doi.org/10.1029/2005WR004025>
- 899 Wilcock, P. R. (1993). Critical Shear Stress of Natural Sediments. *Journal of*
900 *Hydraulic Engineering*, 119(4), 491–505. [http://doi.org/10.1061/\(ASCE\)0733-](http://doi.org/10.1061/(ASCE)0733-9429(1993)119:4(491))
901 [9429\(1993\)119:4\(491\)](http://doi.org/10.1061/(ASCE)0733-9429(1993)119:4(491))
- 902 Wilcox, A. C., Wohl, E. E., Comiti, F., & Mao, L. (2011). Hydraulics, morphology,
903 and energy dissipation in an alpine step-pool channel. *Water Resources*
904 *Research*. <http://doi.org/10.1029/2010WR010192>
- 905 Wong, M., & Parker, G. (2006). Reanalysis and Correction of Bed-Load Relation of
906 Meyer-Peter and Müller Using Their Own Database. *Journal of Hydraulic*
907 *Engineering*. [http://doi.org/10.1061/\(ASCE\)0733-9429\(2006\)132:11\(1159\)](http://doi.org/10.1061/(ASCE)0733-9429(2006)132:11(1159))
- 908 Wong, M., Parker, G., DeVries, P., Brown, T. M., & Burges, S. J. (2007). Experiments
909 on dispersion of tracer stones under lower-regime plane-bed equilibrium bed
910 load transport. *Water Resources Research*.
911 <http://doi.org/10.1029/2006WR005172>
- 912 Yager, E. M., Turowski, J. M., Rickenman, D., & McArdell, B. W. (2012). Sediment
913 supply, grain protrusion, and bedload transport in mountain streams.

914 *Geophysical Research Letters*, 39(10), 1–5.
915 <http://doi.org/10.1029/2012GL051654>
916 Yager, E. M., Venditti, J. G., Smith, H. J., & Schmeeckle, M. W. (2018). The trouble
917 with shear stress. *Geomorphology*, 323, 41-50.
918 <http://doi.org/10.1016/j.geomorph.2018.09.008>

Figure 1.

70° 03' W

33° 45' S

-  Glaciers
-  EM divides
-  EM River
-  Station

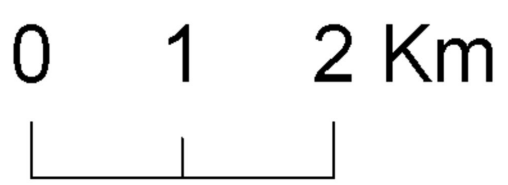
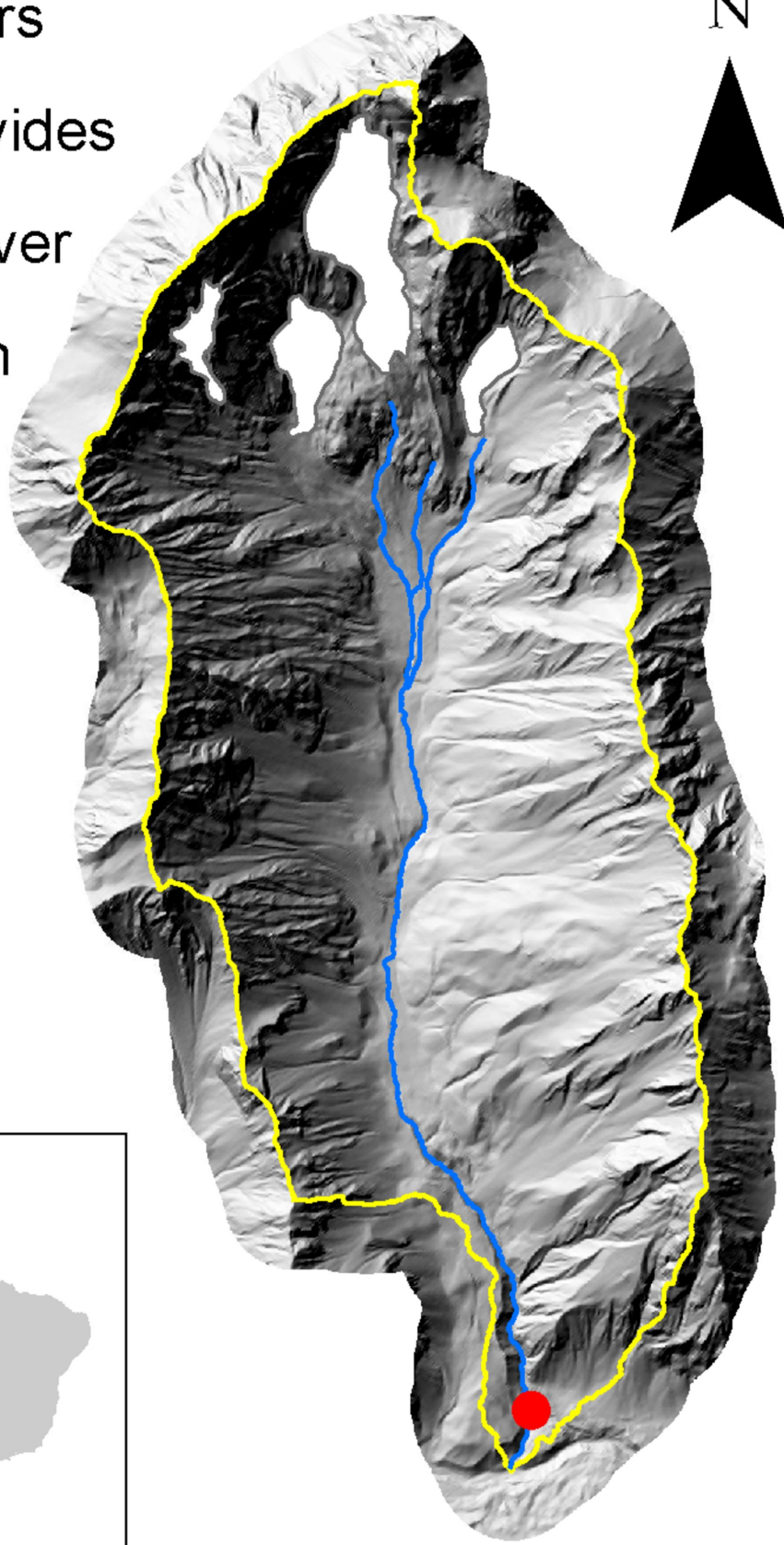


Figure 2.



Figure 3.

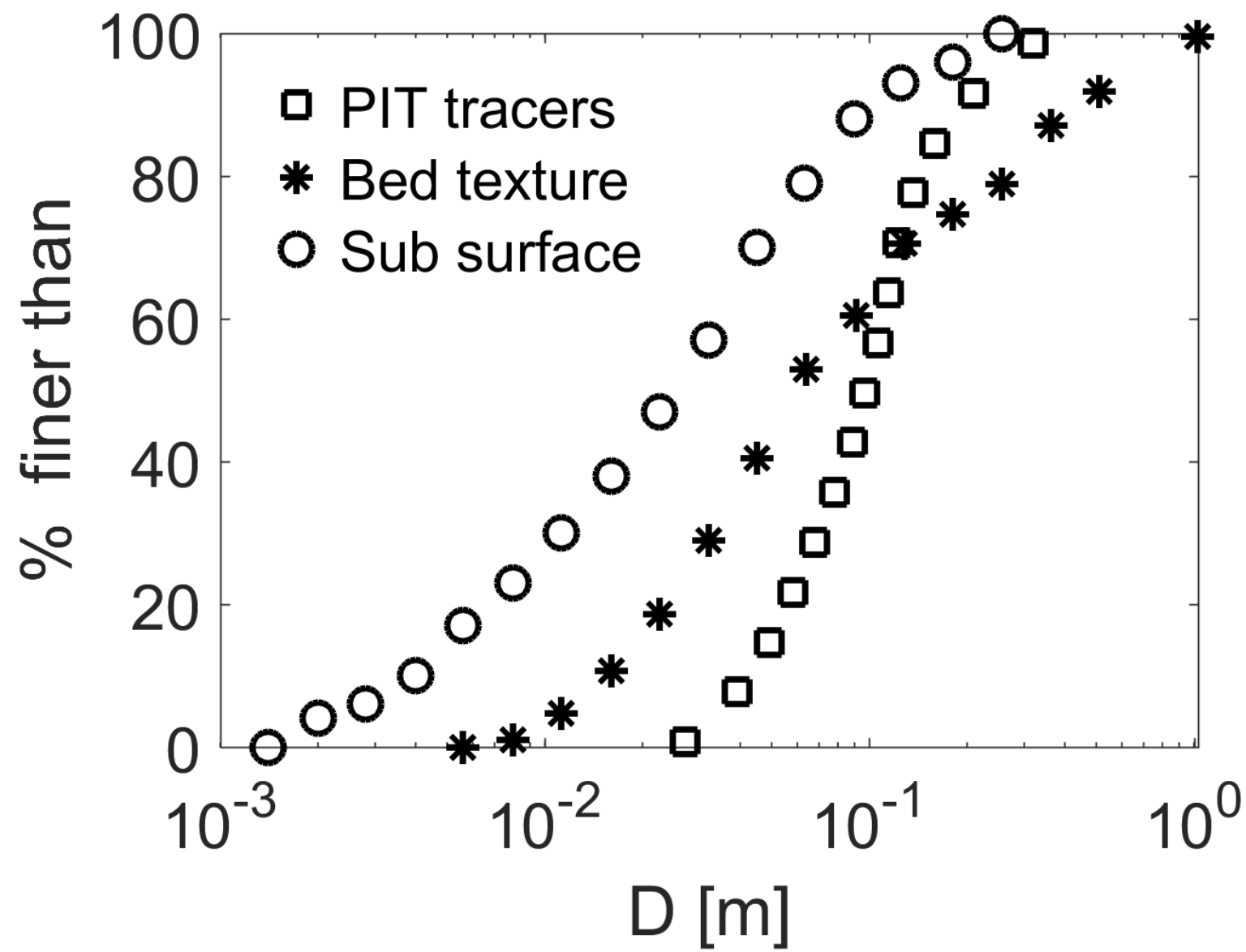


Figure 4.

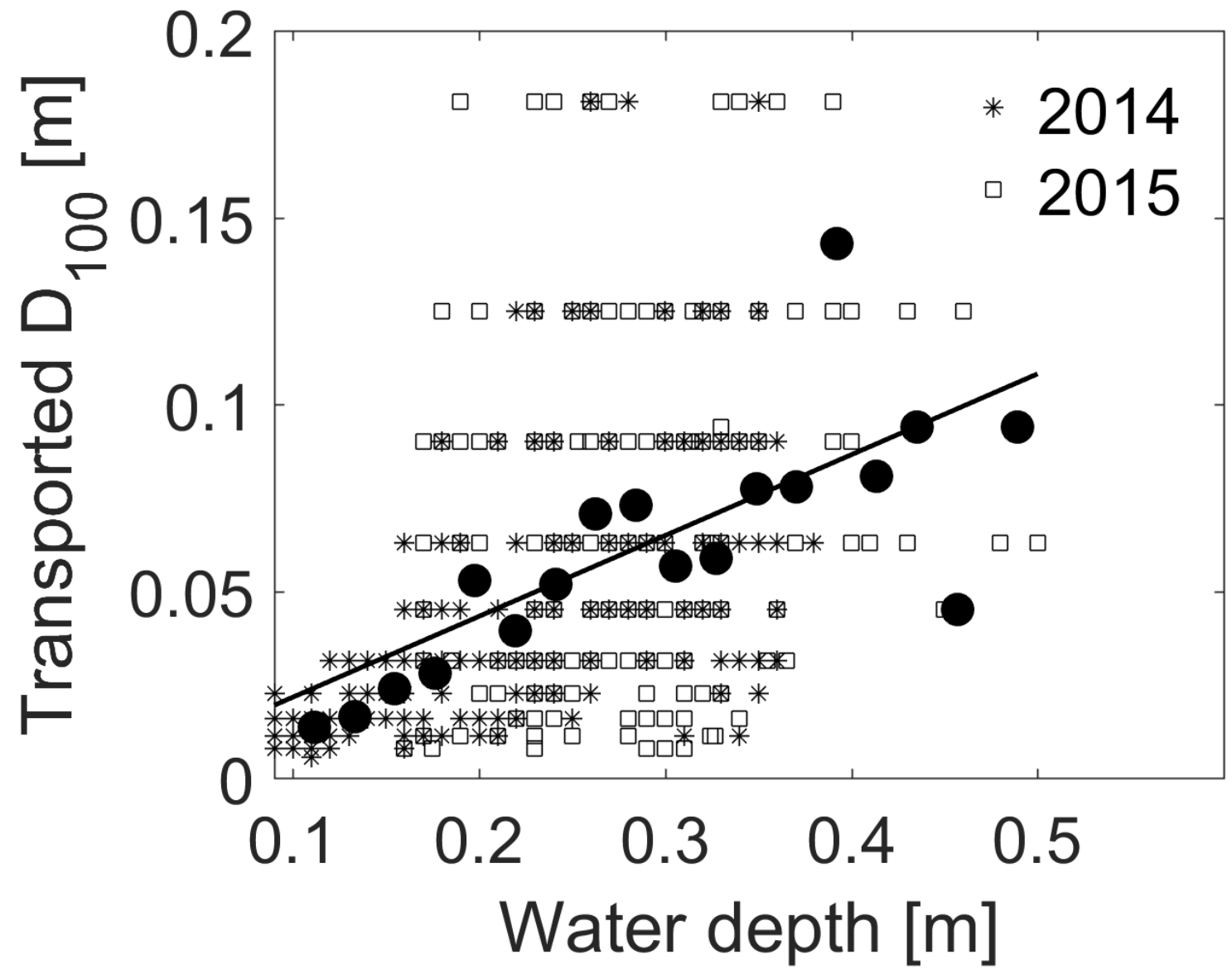


Figure 5.

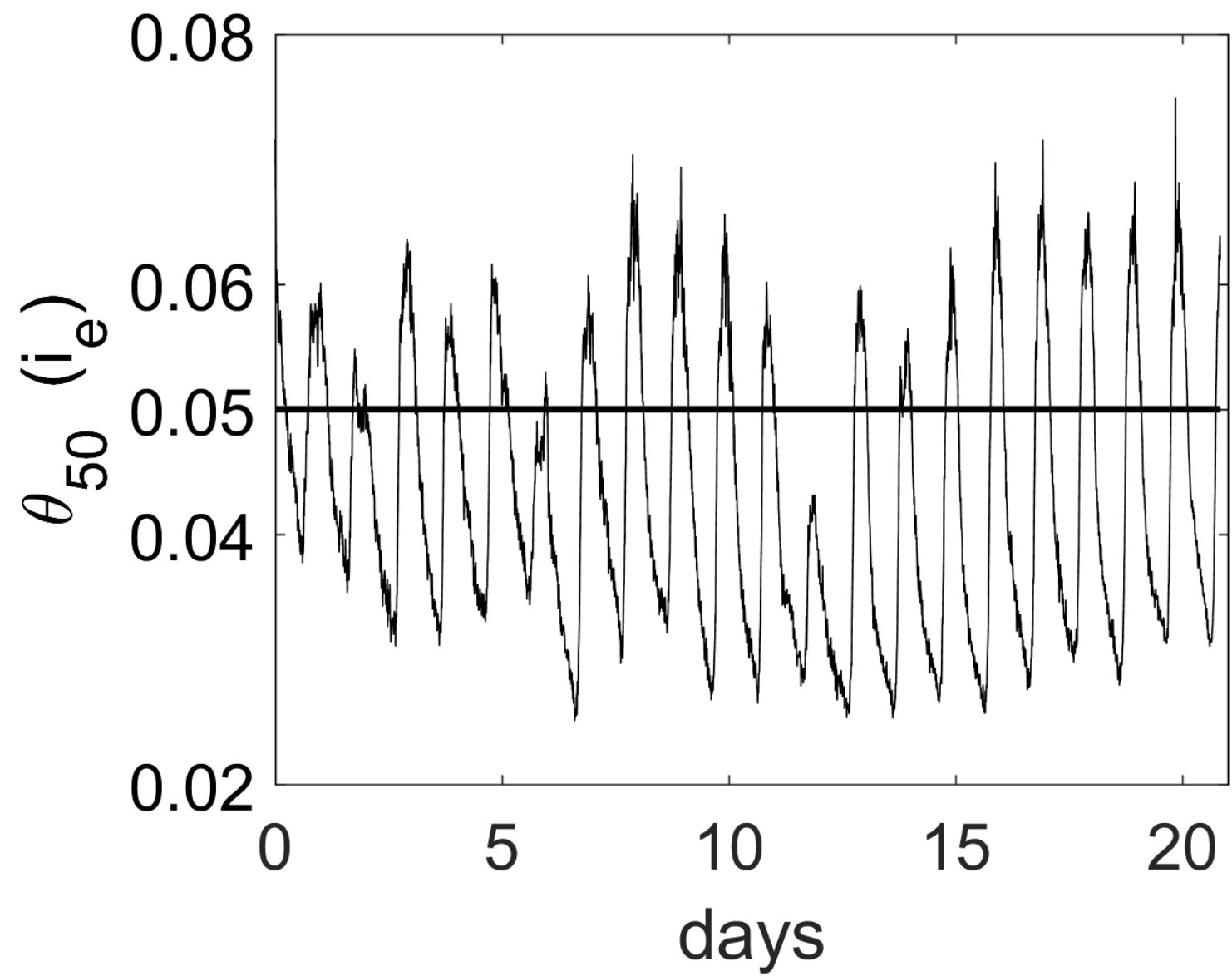


Figure 6.

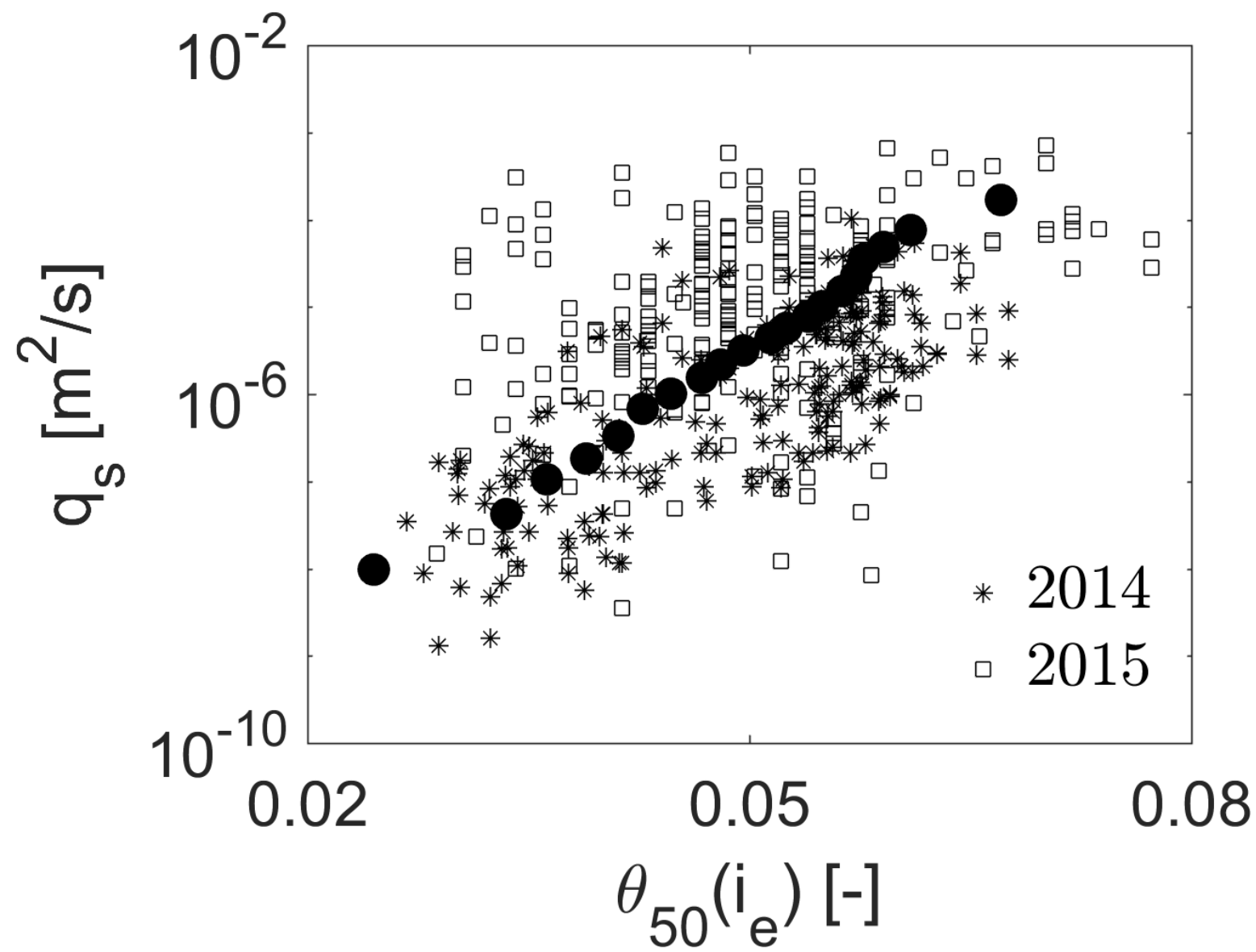


Figure 7.

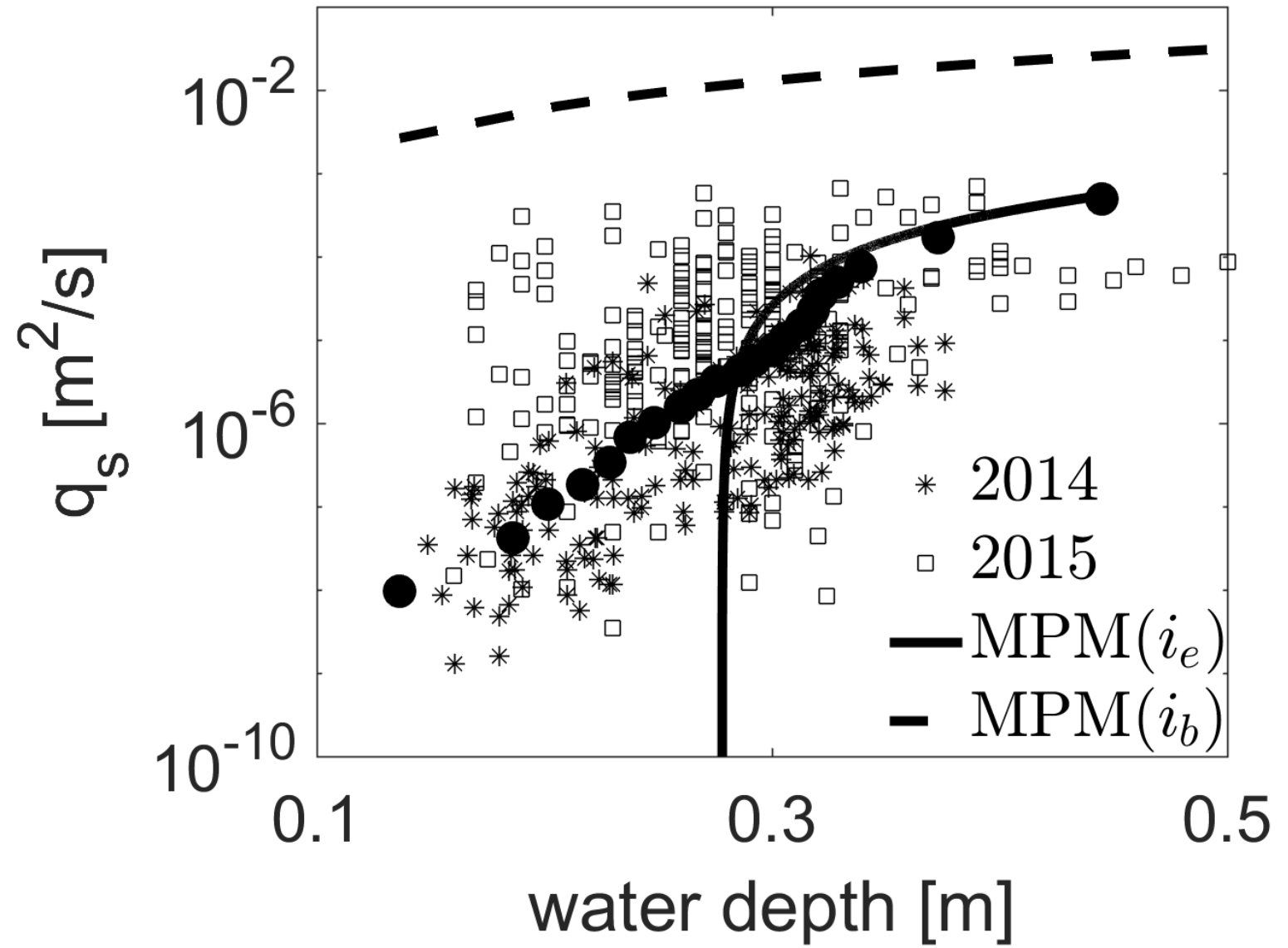


Figure 8.

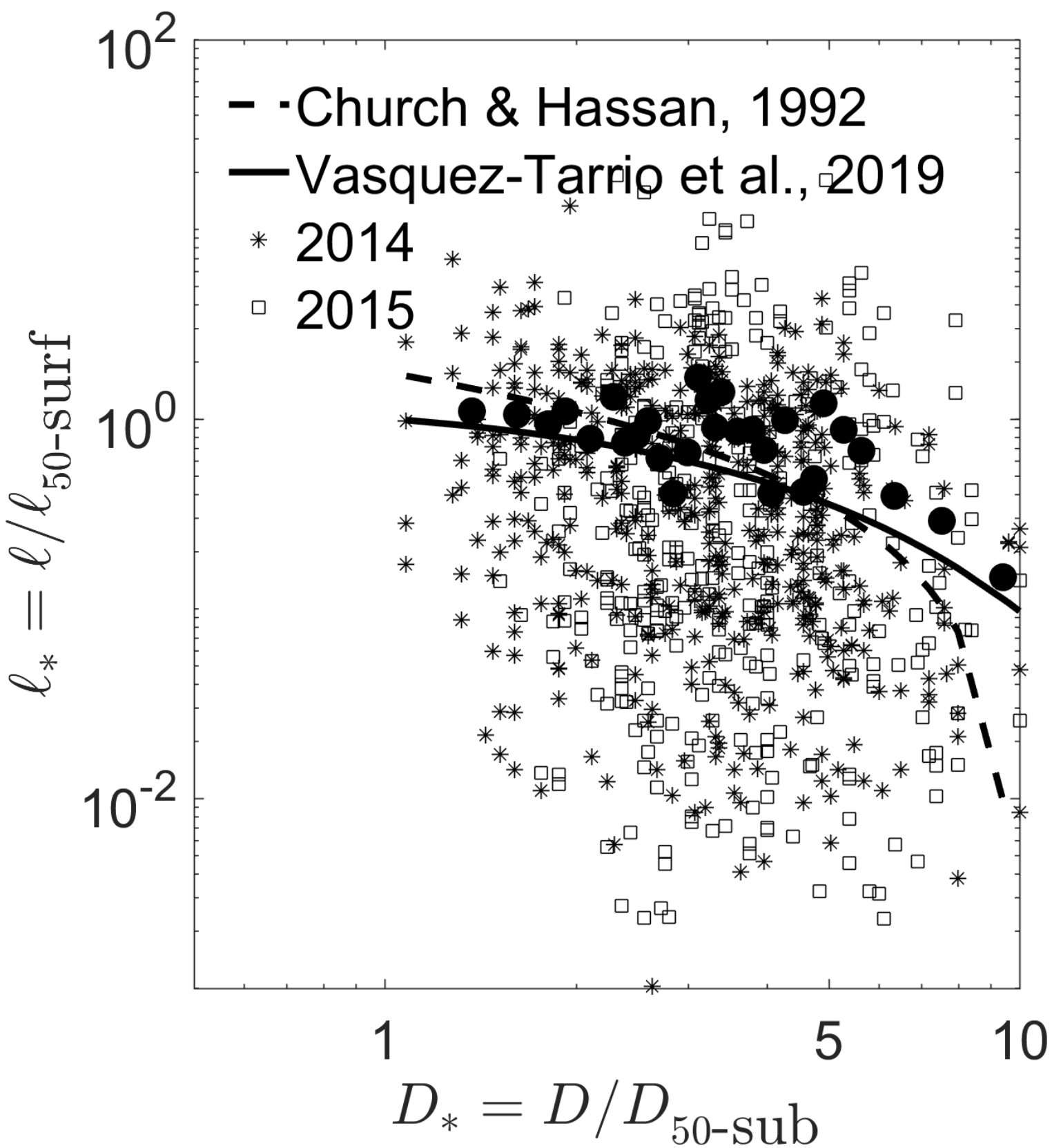


Figure 9.

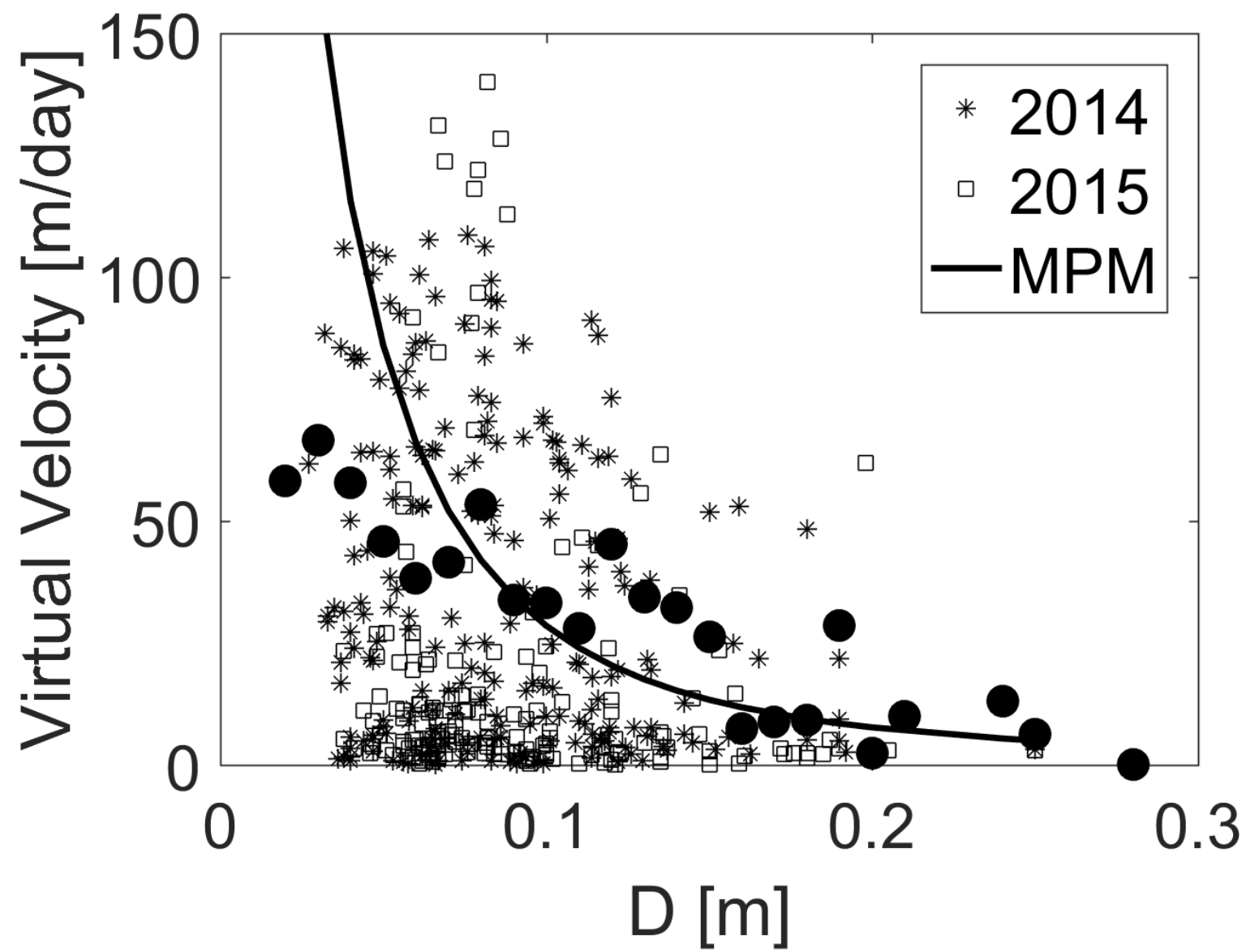


Figure 10.

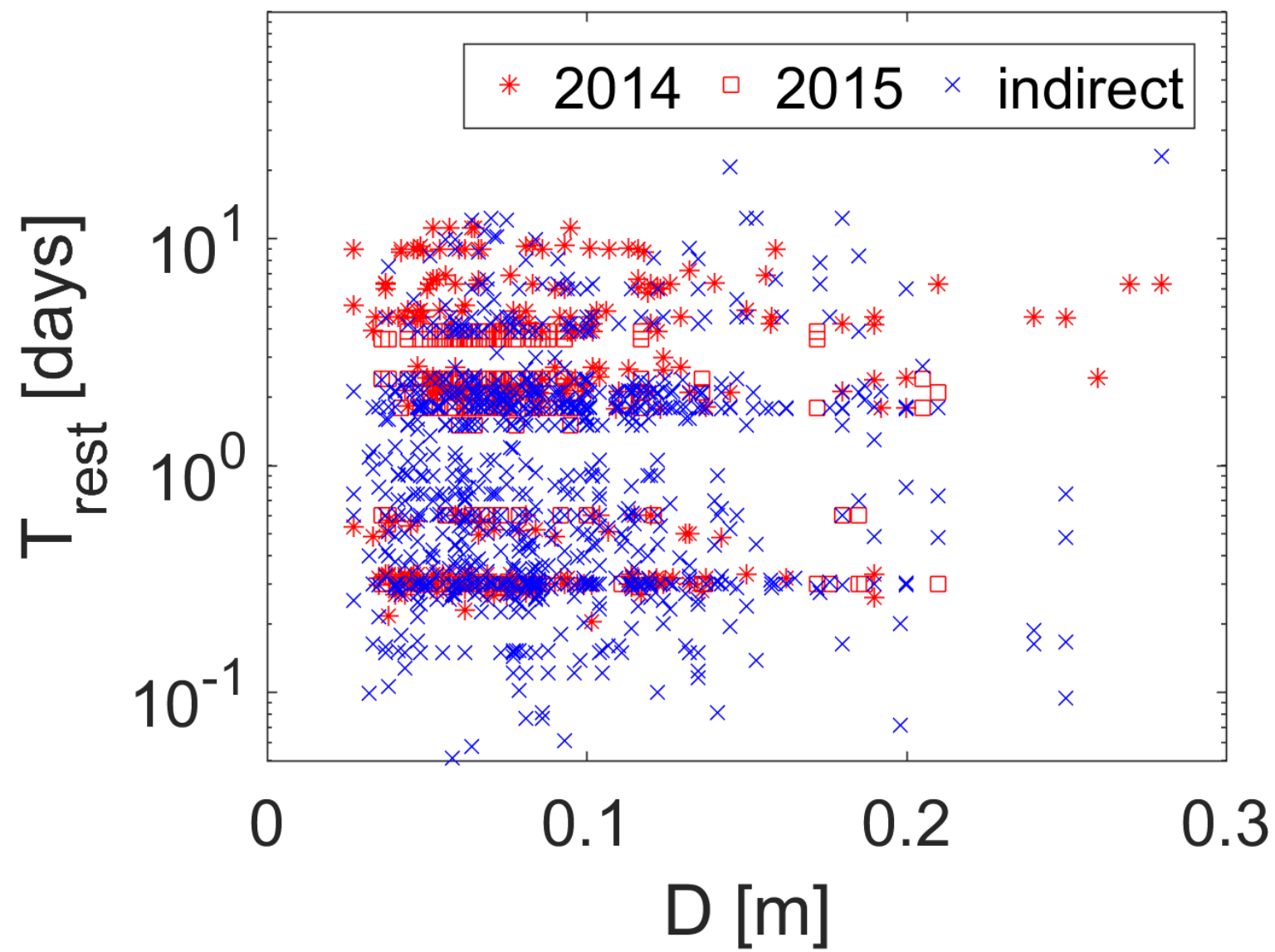


Figure 11.

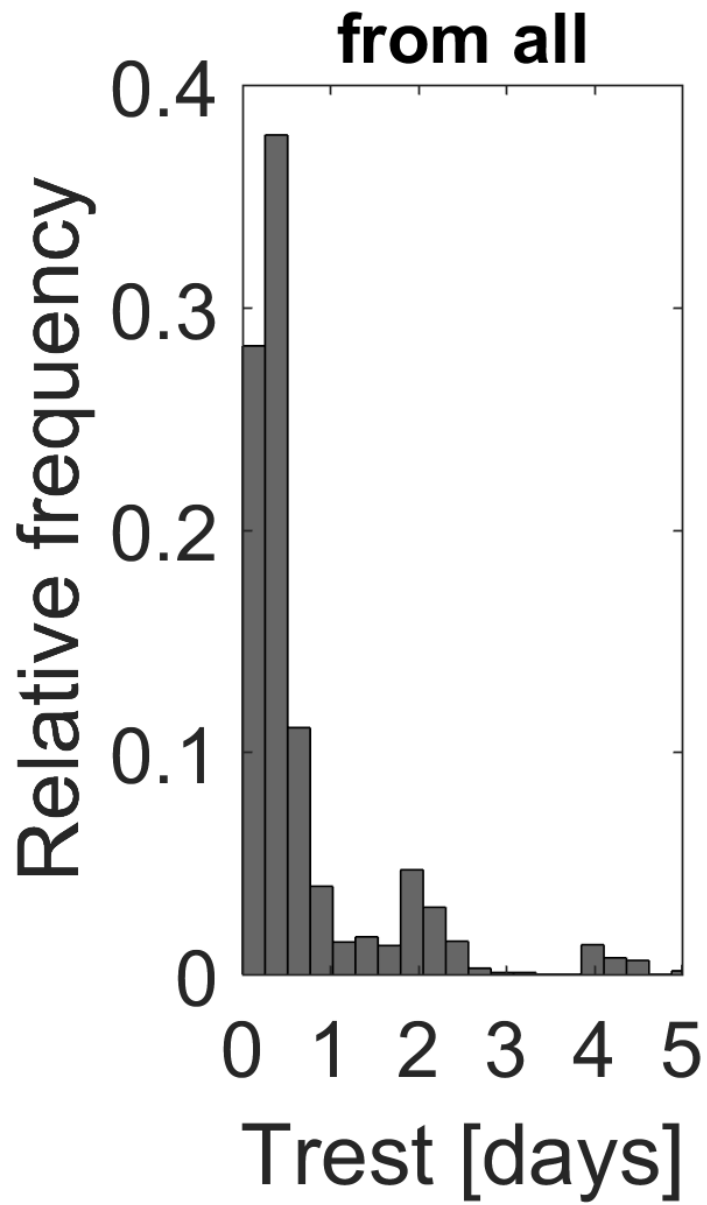
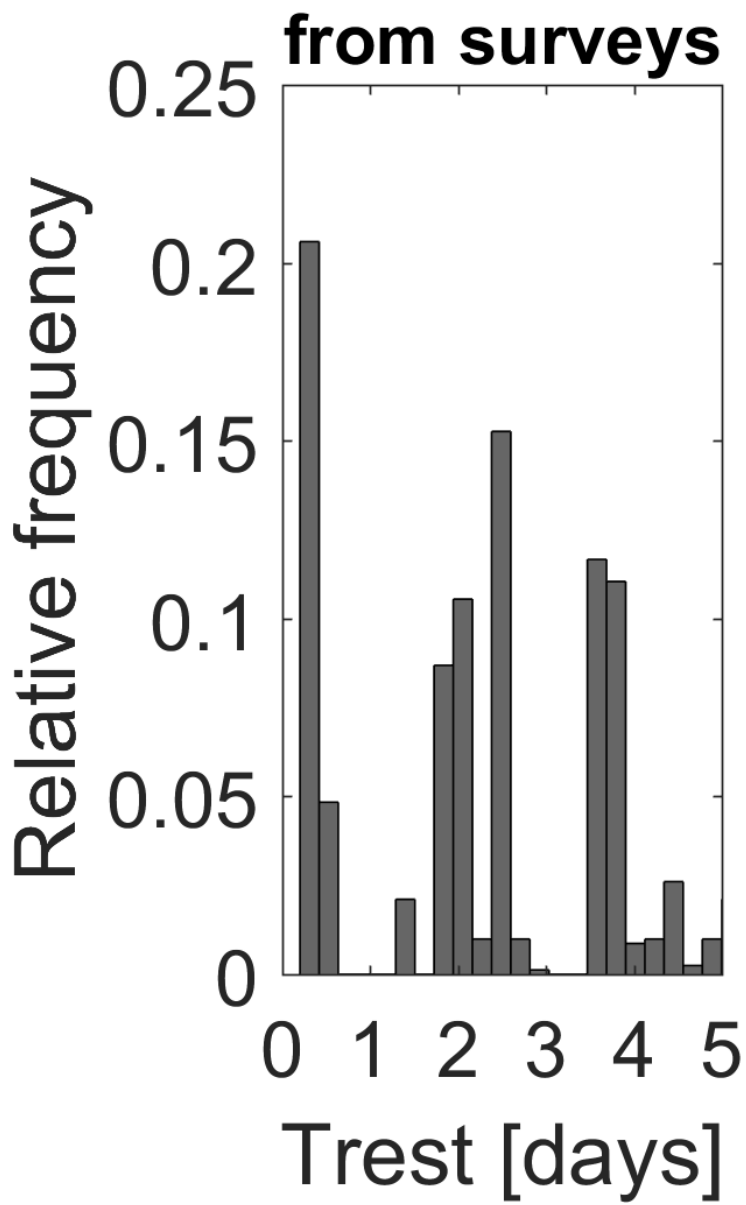


Figure 12.

